Viscoplastic dam-breaks

Rudy Valette, Anselmo Soeiro Pereira, S. Riber, Lucas Sardo, Aurélien Larcher, Elie Hachem

Viscoplastic dam-breaks

R. Valette, A. Pereira, S. Riber, L. Sardo, A. Larcher,

E. Hachem

MINES ParisTech, Centre for material forming (CEMEF), UMR CNRS 7635, CS 10207, 06904, Sophia Antipolis Cedex, France

Abstract

We analyse through numerical simulations, experiments, and scaling laws the dam-break problem for viscoplastic materials. Numerically, both two and three-dimensional (2D and 3D) scenarios are considered thanks to a proposed adaptive stabilized finite element framework able to compute efficiently free surface flows of highly viscoplastic materials. We choose to focus on the Bingham model. Momentum and mass equations are solved by using the Variational MultiScale method coupled with a regularization technique and anisotropic mesh adaptation. A convective self-reinitialization Level-Set method is used to describe the interface evolution. The obtained 2D multiphase results on viscoplastic column collapses show good agreement with literature. Additionally, new 3D simulations for both cylindrical and prismatic columns are explored through energy budget and new scaling laws based on which the collapse process is divided into three regimes: (1) viscous; (2) visco-plastic (mixed); and (3) plastic. These regimes are stressed for a wide range of initial column aspect ratio (1-20) and Bingham number (0.003-0.3). Lastly, the simulations are compared to experiments either taken from existing literature or performed using tailings, mineral suspensions, Carbopol, Mayonnaise, and Ketchup for cylindrical and conical columns.

Key words: viscoplastic material, yield stress material, dam-break flow, numerical simulation, free surface flow, stabilized finite element method, anisotropic mesh adaptation, experiments, scaling law

1 Introduction

In fluid mechanics, viscoplastic models are used to describe materials that ideally behave like a rigid body below a characteristic stress level called *yield stress*, as well as a viscous fluid above the latter. Such models are commonly associated with yield stress materials in flow scenarios for which elasticity, normal stresses and structural time-dependence are negligible and characterized by the coexistence of flowing (yielded) and non-flowing (unyielded) regions (Coussot, 2014; Balmforth et al., 2014; Thompson et al., 2018). In this connection, viscoplastic models have been widely applied in many research fields, such as in geophysics to study avalanches (Huang and Garcia, 1998), magma and mud flows (Ancey, 2007), blood rheology (Venkatesan et al., 2013), as well as in civil engineering to study, for instance, suspensions and/or pastes behaviour (Cremonesi et al., 2010).

When combined with experiments, numerical simulations have proven to be extremely useful for understanding the dynamics of viscoplastic fluids and, consequently, for modelling natural flows and optimizing industrial processes. Nevertheless, accurate representations of such flow patterns remain a challenge in the numerical methods field. Indeed, transitions between yielded and

Email address: anselmo.soeiro_pereira@mines-paristech.fr (A. Pereira).

unyielded regions are still difficult to capture due to the high viscosity jumps occurring. Furthermore, adding an ambient fluid (with a very small viscosity) to free surface flows leads to stiff problems with strong non-linearities, which makes such simulations even more challenging. It is then essential to develop robust and accurate numerical methods in order to solve and represent efficiently non-deformed and deformed regions.

Concerning computational fluid mechanics, both Bingham and Herschel-Bulkley models are the most standard viscoplastic constitutive equations, being characterized by a power-law-like viscous stress that increases beyond a constant (and scalar) yield stress (Bingham, 1916, 1922; Herschel and Bulkley, 1926). Although these models have been extensively studied and simulated by several research teams, few studies concern free surface flows of both Bingham and Herschel-Bulkley fluids in a multiphase framework due to the numerical difficulties of combining interface evolution and high viscosity jumps across the free surface. Among these studies, shallow water approximations were proposed, for instance, by Balmforth et al. (2007) and Matson and Hogg (2007) for predicting the spreading of a Herschel-Bulkley fluid down a slope. These approaches are interesting, but limited to low height profile vs. run-out distance ratio.

Different numerical strategies to overcome the mentioned difficulties have been developed in recent years. Here, some of these strategies are combined and applied to viscoplastic dam-breaks under gravity, an important flow case widely exploited in food, mineral and concrete industries to assess rheological signatures of complex fluids. In this free surface flow situation, a fluid column collapses under gravity and, at stoppage, its spreading level and/or final height are/is measured and linked, for instance, with the yield stress (Pashias et al.,

1996; Schowalter and Christensen, 1998; Clayton et al., 2003; Saak et al., 2004; Roussel and Coussot, 2005; Staron et al., 2013; Pierre et al., 2013; Gao and Fourie, 2015; Liu et al., 2016, 2018; Modolo et al., 2019). Practical variations of this fundamental free surface complex flow include for instance the L-box, a three-dimensional free surface flow of a non-Newtonian fluid between bars as obstacles attached to a L-shape channel used to evaluate the workability of concretes (Nguyen et al., 2006; Roussel, 2007; Chaparian and Nasouri, 2018), and the Bostwick Consistometer, a device widely used to easily recover food product rheological properties and based on a free surface non-Newtonian flow through a channel (Rao and Bourne, 1977; Balmforth et al., 2007).

Two-dimensional simulations on Bingham collapses were performed by Vola et al. (2004) who used the finite element method. Momentum equations were solved using a decomposition-coordination method, avoiding the use of any regularization method. This method consists in relaxing constrains by introducing Lagrange multipliers and then solving a saddle point problem (Saramito and Wachs, 2017). The interface was tracked and then reconstructed by using polygonal curves, at each time step. This method is able to simulate flow arrests, as no regularized viscosity is computed. However, it leads to larger computational times as an additional loop is needed and infeasible in 3D. Additional simulations on two-dimensional Bingham collapses were addressed by Staron et al. (2013) by using a volume of fluid method (VOF). The constitutive equations were considered into the momentum equations by using a regularization method. Specifically, they chose to limit the viscosity by directly introducing a maximum viscosity η_{max}, and considering a ratio between maximum viscosity and plastic viscosity of 10^2. According to Staron et al. (2013) this choice for η_{max} does not affect the results. However, the authors did not

extend their formulation to flow scenarios related to high Bingham numbers Bn (defined as the ratio between yield stress and gravity stress), for which flow arrests can be difficult to determine. Liu et al. (2016) also performed two-dimensional Bingham collapses by using the VOF method and regularization or augmented Lagrangian methods, showing comparable results between the two methods. More recently, these results were extended to axisymmetric Bingham dam-breaks by Liu et al. (2018). Both two and three-dimensional free-surface flows of a Bingham fluid (with regularization) were also considered by Franci and Zhang (2018), who reported a good agreement between numerical results based on a purely Lagrangian framework and few experimental ones. Capillary force effects on the referred flow were taken into account by Nikitin et al. (2011) through a Level-set based method for capturing the free surface evolution, which shown a satisfactory qualitative agreement with experimental results. Nevertheless, more extensive numerical/experimental comparisons are still needed.

Literature then shows that some attempts on the numerical simulation of multiphase viscoplastic dam-break flows have been conducted. However, it is important to emphasise that just a small number of them were devoted to three-dimensional flows up to now and, consequently, many aspects of this topic remain unclear, which includes the suitability of different numerical methods for capturing the physical mechanisms that drive viscoplastic dam-break problems. In addition, since the majority of the reported three-dimensional-based works was focused on the development of numerical tools, numerous fundamental points concerning viscoplastic dam-breaks still need to be addressed, such as: (1) morphological effects of the fluid column on the dam-break dynamics; (2) the existence of distinct columns collapse regimes and their scaling

laws; (3) and the ability of these scaling laws to predict numerical/experimental results.

Aiming to highlight the challenging topics underlined above, we present here a detailed study devoted to viscoplastic dam-breaks under gravity combining numerical simulations, experiments and theoretical analyses. First, we focus on a proposed finite element framework which, in a second step, is applied to two (2D) and three-dimensional (3D) dam-break viscoplastic flows. More specifically, we carefully describe our numerical tools, which includes a regularization method for the Bingham rheology and a Level-Set method used to follow the viscoplastic fluid/air interface during the flow, as well as to handle large topology changes. The resolution framework based on the Variational MultiScale method is then introduced, followed by an anisotropic mesh adaptation technique. Subsequently, the proposed numerical framework is applied to 2D and 3D viscoplastic dam-breaks. Concerning the 3D flow cases, both cylindrical and prismatic columns are taken into account and analysed through energy budget and scaling laws. As a result, three collapse regimes are identified: (1) viscous; (2) visco-plastic (mixed); and (3) plastic. These regimes are stressed for a wide range of initial column aspect ratio (1-20) and Bingham number (0.003-0.3). Lastly, the simulations are compared to a non-exhaustive list of experiments either taken from existing literature or performed using tailings (pastes), mineral suspensions, Carbopol (aqueous suspension), Mayonnaise (concentrated emulsion), and Ketchup (organic suspension) for cylindrical and conical columns.

The organization of the paper is as follows. A detailed description of the physical formulation and numerical method is presented in Section 2. Impatient readers, as well as those who are unfamiliar with numerical methods, could

skip Section 2, jumping directly to Sections 3 and 4, in which the proposed numerical framework is applied to both 2D and 3D viscoplastic dam-break flows and then compared to experiments. Finally, conclusions are drawn in the closing section.

2 Physical formulation and numerical methods

The initial goal in the present work is to present in details a numerical framework capable to correctly capture the physical complexities related to multiphase solenoidal flows of highly viscoplastic materials. In this regard, we first introduce a regularized Bingham constitutive model, which is subsequently injected into the Momentum equations and then solved by using a Variational MultiScale method couple with a anisotropic mesh adaptation, as well as a convective self-reinitialization Level-Set method devoted to interfaces evolution.

Despite the complexity involving the implementation and the subsequent assemblage of the numerical tools presented here, it is important to emphasise that, by using the resulting framework, one can easily explore not only fundamental non-Newtonian multiphase flows (such as dam-breaks, the impact of non-Newtonian drops on solid and liquid, the stretch/compression of non-Newtonian filaments, the development of buckling instabilities ...), but also industrial ones. In other words, the strengths of these numerical methods emerge from their high flexibility/adaptability in taking into account complex flow configurations.

2.1 Constitutive equations

2.1.1 Regularized Bingham constitutive equation

The Bingham constitutive equation is defined as

$$\begin{cases} \boldsymbol{\tau} = \left(k + \frac{\tau_0}{||\dot{\boldsymbol{\gamma}}||}\right)\dot{\boldsymbol{\gamma}} & \text{if } || \boldsymbol{\tau} ||> \tau_0\,, \\ \dot{\boldsymbol{\gamma}} = 0 & \text{if } || \boldsymbol{\tau} ||\leq \tau_0\,, \end{cases} \tag{1}$$

where $\boldsymbol{\tau}$, τ_0 and k are the extra-stress tensor (written as a Generalized Newtonian Fluid, i.e. $\boldsymbol{\tau} = \eta\dot{\boldsymbol{\gamma}}$, where $\dot{\boldsymbol{\gamma}}$ is the rate-of-strain tensor defined as $\dot{\boldsymbol{\gamma}} = \boldsymbol{\nabla u} + \boldsymbol{\nabla u}^T$, and η is the material viscosity), the yield stress and the fluid consistency (also called in the literature 'plastic viscosity' and 'viscous parameter of the Bingham model', Thompson and Soares, 2016). Additionally, $|| \dot{\boldsymbol{\gamma}} ||$ denotes the deformation rate, being defined as

$$|| \dot{\boldsymbol{\gamma}} ||= \left(\frac{1}{2}\dot{\boldsymbol{\gamma}} : \dot{\boldsymbol{\gamma}}\right)^{\frac{1}{2}}\,, \tag{2}$$

where $\dot{\boldsymbol{\gamma}} : \dot{\boldsymbol{\gamma}} = \sum_{i,j} \dot{\gamma}_{ij}\dot{\gamma}_{ij}$. Analogously, the norm of the extra-stress tensor $\boldsymbol{\tau}$ reads

$$|| \boldsymbol{\tau} ||= \left(\frac{1}{2}\boldsymbol{\tau} : \boldsymbol{\tau}\right)^{\frac{1}{2}}\,. \tag{3}$$

In this formulation, the viscosity of the non-Newtonian fluid phase, also called Bingham viscosity, is defined above the yield stress such as

$$\eta = k + \frac{\tau_0}{||\dot{\boldsymbol{\gamma}}||} \,. \tag{4}$$

The resolution of momentum equations leads to an ill-posed problem as the Bingham viscosity is not defined in the unyielded areas. Consequently, the main challenge consists in taking into account the constitutive law into motion and mass equations. In this work, we use a regularization method, based on the use of the Bingham viscosity related to the viscous fluid phase. When the rate-of-strain is non zero, this viscosity must approach the plastic viscosity and when no deformation occurs, it must be as large as possible. Regularization methods aim to control and limit the maximum viscosity, in order to avoid solver convergence problems due to viscosity divergence.

Papanastasiou (1987) proposed a regularization method which consists in bounding the viscosity exponentially in the vicinity of zero rate-of-strain. Thus, we find the following expression for the viscosity η within the Bingham phase

$$\eta = k + \frac{\tau_0}{|| \dot{\boldsymbol{\gamma}} ||}[1 - exp(-\frac{|| \dot{\boldsymbol{\gamma}} ||}{m})] \,, \tag{5}$$

where m corresponds to the Papanastasiou coefficient that controls the yield limit: the lower m, the closer the solution to the Bingham solution. However, as already mentioned, very low values of m may result in uncontrollable oscillations and non-convergence to the solution, in particular for large Bingham numbers.

The Level-Set method, introduced by Osher and Sethian (1988) has been applied to numerous two-fluid flows. It consists first in computing the signed distance function to the interface α. As shown in Fig. $1(a)$, that describes its initial value, this function is positive in Ω_f and negative in Ω_{air}, where Ω denotes the computational fluid domain ($\Omega \subset \mathbb{R}^n$, at time $t \in [0, T]$). The zero value corresponds to the interface between the two sub-domains.

$$\alpha(\boldsymbol{x}) = \begin{cases} d(\boldsymbol{x}, \Gamma) & , \boldsymbol{x} \in \Omega_f \,; \\ -\, d(\boldsymbol{x}, \Gamma) & , \boldsymbol{x} \in \Omega_{air} \,; \\ 0 & , \boldsymbol{x} \in \Gamma \,. \end{cases} \tag{6}$$

Then, we need to follow the interface during the simulation. Thus, the transport equation of the Level-Set function should be solved, giving the new interface location:

$$\begin{cases} \frac{\partial \alpha}{\partial t} + \boldsymbol{v} \cdot \nabla \alpha = 0 \,; \\ \alpha(t = 0, \boldsymbol{x}) = \alpha_0(\boldsymbol{x}) \,. \end{cases} \tag{7}$$

This method is often applied in phase transformation and multiphase flows (Osher and Fedkiw, 2001; Ji et al., 2002). Indeed, it allows to describe a wide range of problems, as it can handle problems where the surface evolves in fairly complex ways with high topology changes. Then, intrinsic geometric properties of the interface, such as normal vectors or curvatures, are determined from

the Level-Set field. However, some additional treatments, listed below, are necessary to improve the efficiency of this approach.

2.2.1 Redistancing and filtering of the Level-Set function

After the resolution of the transport equation (7), many oscillations may appear close to the interface, polluting the interface quality. Indeed, the iso-contours of the Level-Set function are not smooth any more, leading to the loss of its metric property $|| \nabla\alpha ||= 1$. Thus, a reinitialization step is performed by solving the Hamilton-Jacobi equation to ensure $|| \nabla\alpha ||= 1$.

Moreover, during the convection of the Level-Set function, high gradient changes may occur, giving rise to instabilities and then polluting the final solution. Usually, a filtering function $\hat{\alpha}$ is defined, equals to zero at the interface, approaching α close to the interface, and keeping constant value far from the interface. Several filtering functions can be found in the literature (Khalloufi et al., 2016; Olsson and Kreiss, 2005; Bonito et al., 2015). In this work, a hyperbolic tangential filter is used. Thus, the new filtered Level-Set function $\hat{\alpha}$ is computed such as:

$$\hat{\alpha} = E \times tanh\left(\frac{\alpha}{E}\right) \tag{8}$$

E corresponds to the interface *thickness*: figure $1(b)$ shows a typical plot of $\hat{\alpha}$, which tends to E as α increases.

Thus, the reinitialization equations can be updated taking into account the filtered Level-Set function $\hat{\alpha}$. The gradient of $\hat{\alpha}$ is computed such as:

$$\frac{\partial \hat{\alpha}(\alpha)}{\partial \alpha} = 1 - tanh^2\left(\frac{\alpha}{E}\right) \tag{9}$$

and is formulated with respect to $\hat{\alpha}$:

$$\frac{\partial \hat{\alpha}(\alpha)}{\partial \alpha} = 1 - \left(\frac{\hat{\alpha}(\alpha)}{E}\right)^2 \tag{10}$$

Then, a new fictive step, called t_f, is introduced. The purpose consists in finding a new parametric function β where the reinitialization step must be performed, and having the same isovalue α such as

$$|| \nabla \beta || = 1 \,. \tag{11}$$

The Hamilton-Jacobi equation is then formulated such as

$$\begin{cases} \frac{\partial \beta}{\partial t_f} + s(\beta)(||\nabla \beta|| - 1) = 0 \,; \\ \\ \beta(t_f = 0, \boldsymbol{x}) = \alpha(t, \boldsymbol{x}) \,. \end{cases} \tag{12}$$

Considering now the filtering Level-Set function $\hat{\alpha}$, the Hamilton-Jacobi equation becomes

$$\begin{cases} \frac{\partial \beta}{\partial t_f} + s(\hat{\alpha}) \left[||\nabla \hat{\alpha}|| - \left(1 - \left(\frac{\hat{\alpha}}{E}\right)^2\right)\right] = 0 \,; \\ \\ \beta(t_f = 0, \boldsymbol{x}) = \alpha(t, \boldsymbol{x}) \,. \end{cases} \tag{13}$$

By turning equations (13) as a transport equation, the problem is rewritten such as

$$\begin{cases} \frac{\partial \beta}{\partial t_f} + \boldsymbol{U} \cdot \nabla \hat{\alpha} = s(\hat{\alpha}) \left[1 - \left(\frac{\hat{\alpha}}{E} \right)^2 \right] ; \\ \\ \beta(t_f = 0, \boldsymbol{x}) = \alpha(t, \boldsymbol{x}) \, , \end{cases} \tag{14}$$

with

$$\boldsymbol{U} = \frac{s(\hat{\alpha}) \nabla \hat{\alpha}}{|| \nabla \hat{\alpha} ||}.$$

2.2.2 Coupling transport and redistancing steps

We propose to couple both the transport and the Hamilton-Jacobi equations (Khalloufi et al., 2016). This step will reduce the system to finally one global transport equation and will consequently eliminate the frequency parameter for the reinitialization. Thus, we define λ such as the ratio between fictive and real time steps

$$\lambda = \frac{\partial t_f}{\partial t} \, . \tag{15}$$

Then, by choosing λ such as $\lambda = \frac{l}{\triangle t}$, where l is the mesh size, one obtains

$$\frac{\partial \beta}{\partial t} = \lambda \frac{\partial \beta}{\partial t_f} \, . \tag{16}$$

Introducing equation (16) in equation (14), the new convection-reinitialization equation is obtained

$$\frac{\partial \beta}{\partial t} + \lambda \boldsymbol{U} \cdot \nabla \hat{\alpha} = \lambda s(\hat{\alpha}) \left[1 - \left(\frac{\hat{\alpha}}{E} \right)^2 \right] . \tag{17}$$

Therefore, in particular at the interface, the equation that couples the transport and the reinitialization steps will be formulated as follows

$$\frac{\partial \hat{\alpha}}{\partial t} + (\boldsymbol{v} + \lambda \boldsymbol{U}) \cdot \nabla \hat{\alpha} = \lambda s(\hat{\alpha}) \left[1 - \left(\frac{\hat{\alpha}}{E} \right)^2 \right] . \tag{18}$$

This new equation leads to the appearance of a new convection term: $(\boldsymbol{v} + \lambda \boldsymbol{U}) \cdot \nabla \hat{\alpha}$. The associated variational formulation is: find $\hat{\alpha} \in \mathcal{L}^2(\Omega)$ such that

$$\left(\frac{\partial \hat{\alpha}}{\partial t}, \Phi \right)_\Omega + [(\boldsymbol{v} + \lambda \boldsymbol{U}) \cdot \nabla \hat{\alpha}, \Phi]_\Omega = \left[\lambda s(\hat{\alpha}) \left(1 - \left(\frac{\hat{\alpha}}{E} \right)^2 \right), \Phi \right]_\Omega \tag{19}$$

for all $\Phi \in \mathcal{L}^2(\Omega)$.

The problem is then discretized with respect to time by using a BFD2 method. Finally, the discretized problem is

$$\left(\frac{3\hat{\alpha}^{n+1} - 4\hat{\alpha}^n + \hat{\alpha}^{n-1}}{2\Delta t}, \Phi \right)_\Omega + \left[(\boldsymbol{v} + \lambda \boldsymbol{U}) \cdot \nabla \hat{\alpha}^{n+1}, \Phi \right]_\Omega = \left[\lambda s(\hat{\alpha}^n) \left(1 - \left(\frac{\hat{\alpha}^n}{E} \right)^2 \right), \Phi \right]_\Omega . \tag{20}$$

2.3 Method of resolution

2.3.1 Momentum and mass equations

The numerical simulation of viscoplastic flows leads to the resolution of momentum and mass equations (analogue to the incompressible Navier-Stokes

equations for Newtonian fluids). The computational fluid domain is defined such as $\Omega \subset \mathbb{R}^n$, at time $t \in [0, T]$. This problem consists in finding velocity and pressure fields (v and p), defined respectively in the spaces $V = \mathbb{R}^n$, $P = \mathbb{R}$, such that

$$\begin{cases} \rho \left(\frac{\partial \boldsymbol{v}}{\partial t} + \boldsymbol{v} \cdot \nabla \boldsymbol{v} \right) + \nabla p - \nabla \cdot \boldsymbol{\tau} = \boldsymbol{f} \,, \\ \nabla \cdot \boldsymbol{v} = 0 \,, \end{cases} \tag{21}$$

where $\boldsymbol{\tau}$ and $\boldsymbol{f}$ correspond respectively to the extra-stress tensor and the source term. Recall that the viscous fluid and air densities (ρ_f and ρ_{air}) and viscosities (η_f and η_{air}) are mixed (into ρ and η, respectively) and computed using the Heaviside function of the filtered LevelSet $H(\hat{\alpha})$.

2.3.2 The Variational MultiScale method

As it is well known, the stability of the discrete formulation depends on appropriate compatibility restrictions for the choice of finite element spaces. In this section, a Variational MultiScale (VMS) method is introduced, initially proposed by Hugues (1995); Hugues et al. (1998, 2006), which enables the use of equal order continuous interpolations while preventing from oscillations due to convection dominated flows. Indeed, it offers an ideal framework to deal accurately with different physics such as Darcy flows (Nakshatrala et al., 2006), fluid-structure interaction (Hachem et al., 2013), hydrodynamics (Scovazzi, 2012; Houzeaux et al., 2009), multiphase flows (Lins et al., 2010; Elias and Coutinho, 2007), non-Newtonian fluids flows (Castillo and Codina, 2014) and more. For more details on the proposed VMS method for this work, the

reader may refer to Hachem et al. (2010).

The Variational MultiScale method consists in decomposing pressure and velocity spaces as $P_l \oplus P'$ and $V_l \oplus V'$. Subscript l is used to denote the finite element (coarse) component, and the prime is used for the so-called sub-grid scale (fine) component. According to that, the problem unknowns $\boldsymbol{v}$ and p are split likewise

$$\begin{aligned} \boldsymbol{v} &= \boldsymbol{v_l} + \boldsymbol{v'} \in V_l \oplus V' \,, \\ p &= p_l + p' \ \in P_l \oplus P' \,. \end{aligned} \tag{22}$$

According to that, the weak formulation of Navier-Stokes problem turns then into: find $(\boldsymbol{v_l} + \boldsymbol{v'}, p_l + p') \in V_l \oplus V' \times P_l \oplus P'$ such that

$$\begin{cases} [\rho \partial_t (\boldsymbol{v_l} + \boldsymbol{v'}), \boldsymbol{w_l} + \boldsymbol{w'}] \ + [\rho(\boldsymbol{v_l} + \boldsymbol{v'}) \cdot \nabla(\boldsymbol{v_l} + \boldsymbol{v'}), \boldsymbol{w_l} + \boldsymbol{w'}] \\ - [p_l + p', \nabla \cdot (\boldsymbol{w_l} + \boldsymbol{w'})] \ + [2\eta \dot{\boldsymbol{\gamma}}(\boldsymbol{v_l} + \boldsymbol{v'}) : \dot{\boldsymbol{\gamma}}(\boldsymbol{w_l} + \boldsymbol{w'})] = (f, \boldsymbol{w_l} + \boldsymbol{w'}) \,, \\ [\nabla \cdot (\boldsymbol{v_l} + \boldsymbol{v'}), q_l + q'] = 0 \ , \end{cases} \tag{23}$$

for all $(\boldsymbol{w_l} + \boldsymbol{w'}, q_l + q') \in V_l \oplus V' \times P_l \oplus P'$. Following the lines in Codina (1998) and Codina and Principe (2007), the small scale problem is modelled and then reinjected into the large scale problem. This introduces additional residual terms that insures stability as follows

$$\begin{cases} (\rho\partial_t \boldsymbol{v_l}, \boldsymbol{w_l}) & + [\rho \boldsymbol{v_l} \cdot \nabla(\boldsymbol{v_l} + t_a \mathcal{R}_a), w_l] - (p_l + \tau_b \mathcal{R}_b, \nabla \cdot \boldsymbol{w_l}) \\ & + [2\eta \dot{\boldsymbol{\gamma}}(\boldsymbol{v_l}), \dot{\boldsymbol{\gamma}}(\boldsymbol{w_l})] = (\boldsymbol{f}, \boldsymbol{w_l}) \, , \\ [\nabla \cdot (\boldsymbol{v_l} + t_a \mathcal{R}_a), q_l] = 0 \ , \end{cases} \tag{24}$$

where

$$\begin{aligned} \mathcal{R}_a &= \boldsymbol{f} - \nabla \cdot [2\eta \dot{\boldsymbol{\gamma}}(\boldsymbol{v_l})] - \nabla p_l - (\rho \boldsymbol{v_l} \cdot \nabla \boldsymbol{v_l}) - \rho \partial_t \boldsymbol{v_l} \, , \\ \mathcal{R}_b &= -\nabla \boldsymbol{v_l} \, , \end{aligned} \tag{25}$$

t_a and t_b correspond to the stabilization coefficients, defined as follow

$$t_1 = \left[\left(\frac{4\eta}{h^2} \right)^2 + \left(2\rho \frac{|| \, \boldsymbol{v_l} \, ||}{h} \right)^2 \right]^{-1/2} , \tag{26}$$

$$t_2 = \left[\left(\frac{\eta}{\rho} \right)^2 + \left(\frac{c_b}{c_a} \frac{|| \, \boldsymbol{v_l} \, ||}{h} \right)^2 \right]^{1/2} , \tag{27}$$

where l is the characteristic length of the element (see Codina and Principe, 2007, for details)).

2.3.3 Anisotropic mesh adaptation

In order to resolve localized physical phenomenon, we rely on a reliable and efficient mesh adaptation strategy. It is based on a posteriori error analysis for different fields simultaneously to build a metric tensor for anisotropic mesh adaptation (Riber et al., 2016; Roquet and Saramito, 2003; Valette et al., 2019; Pereira et al., 2019, 2020). Therefore, the shape sizes and the orientation of

the elements will account automatically and dynamically for high gradients in particularity at the interface and efficiently will describe the transition between yielded and unyielded regions (see section 4 for details). The difference with classical approaches resides in dealing with several fields simultaneously by defining one vector of sources of error:

$$\mathbf{v}(\mathbf{x}^i) = \left\{ \frac{\hat{\alpha}}{E}, \frac{v^i}{||v^i||}, \frac{||v^i||}{\max\limits_j ||v^j||}, \frac{\eta}{\max(\eta)} \right\} \tag{28}$$

3 Problem statement: numerical and experimental viscoplastic dam-break flows

The dam-break problem is the collapse of a fluid column under gravity. As exposed previously, this canonical flow is commonly considered in several industrial domains as a very simple and attractive method to estimate rheological properties of non-Newtonian materials. The problem statement is illustrated in Fig. 2. In the present work, we analyse viscoplastic dam-breaks not only by applying the numerical framework detailed in Section 2, but also experimentally.

Numerically, as shown in Fig. 2(a), we consider a computational domain with height H and length/depth L occupied by two materials: a viscoplastic fluid (in red); and air (in blue). The viscoplastic fluid initially occupies a 2D rectangular (Fig. 2b), a 3D cylindrical (Fig. 2c) or a 3D prismatic region (Fig. 2d) with initial height h_0 ($h_0 = z_0$), initial length or radius r_0 ($r_0 = x_0 = y_0$), and volume V, while the air occupies the rest of the domain. No-slip boundary conditions are applied on the bottom wall, and symmetric conditions, at the

left wall (in 2D) and left/front walls (in 3D). Dynamic wetting of the bottom wall by the viscoplastic fluid must be ensured onto the bottom surface in order to avoid triple point (in 2D) and triple line (in 3D) flow singularity. Thus, we set a slip boundary condition on a thin viscoplastic fluid layer at an upstream distance ϵ_g (of the order of the minimum mesh size l_{min}) from the front flow. At the end of the collapse process (stoppage), the viscoplastic material exhibits a final height h_∞ ($h_\infty = z_\infty$) and final front position r_∞ ($r_\infty = x_\infty = y_\infty$), as illustrated in Fig. 2(e).

The initial aspect ratio a is defined as the ratio between the initial height and radius of the column $a = h_0/r_0$. Furthermore, equations are scaled using the characteristic length h_c, stress τ_c, and velocity U_c. The first two terms are defined as $h_c = h_0$, and $\tau_c = \rho g h_0$. The characteristic velocity, in turn, emerges from the energy conservation principle, according to which the initial gravitational potential energy of the fluid column is transferred into kinetic energy and viscous dissipation during the collapse:

$$\rho g h_0 \sim \frac{\rho U_c^2}{2} + k\left(\frac{U_c}{h_c}\right) + \tau_0\,. \tag{29}$$

In the present study, we only take into account numerical Bingham dam-breaks with negligible inertial effects (this will be shown in details through energy budget curves in following Sections). As a result, the characteristic velocity reads $U_c = (h_0/k)\,(\rho g h_0 - \tau_0)$, which scales with the driving potential for flow $\rho g h_0 - \tau_0$. A characteristic time is then defined as $t_c = h_0/U_c = k/\,(\rho g h_0 - \tau_0)$. Noticeable, dimensionless quantities are then $\bar{h} = h/h_0$ ($= z/h_0$) for the dimensionless height, $\bar{r} = r/r_0$ ($= x/r_0 = y/r_0$) for the dimensionless front position, and $\bar{t} = t/t_c$ for the dimensionless time. Finally, $\bar{h}_\infty = h_\infty/h_0$ for

the dimensionless final height, $\bar{r}_\infty = r_\infty/r_0$ for the dimensionless final front position, and $\mathrm{Bn} = \tau_0/\tau_c = \tau_0/(\rho g h_0)$ for dimensionless yield stress, also called Bingham number.

Figures 2(b), 2(c), and 2(d) also illustrate the initial meshing with respect to the Level-Set function (black line in the blue $y-z$ plane). The high number of mesh elements at the viscoplastic fluid/air interface plays a major role for the correct description of the large topology chances observed during the collapse process. For the 2D cases, the number of mesh elements per column unit area is 25x10^4 m^{-2}, while, for the 3D cases, the number of mesh elements per column unit volume is 25x10^6 m^{-3} (a sensitivity analysis is available in Appendix). The mesh is adapted several times until one obtains an optimal mesh close to the interface. The flow cases simulated in the present work are summarised in Table 1.

Table 1

Viscoplastic dam-break flow cases simulated in the present work.

column	h_0/r_0	g [m/s^2]	ρ [kg/m^3]	k [Pa s]	τ_0 [Pa]	Bn
2D rectangular	1-20	1000	0.001	1	0.003-0.3	0.003-0.3
3D cylindrical	1-20	1000	0.001	1	0.003-0.3	0.003-0.3
3D prismatic	1-20	1000	0.001	1	0.003-0.3	0.003-0.3

In order to complement our analyses, we not only carry out experiments using aqueous suspension of Carbopol (aqueous suspension), Mayonnaise (concentrated emulsion), and Ketchup (organic suspension), but also compare our numerical/experimental results to experiments available in the literature, with includes tailings (pastes) and mineral suspensions. The details regarding the

considered fluids/experiments are displayed in Table 2.

In general terms, dam-break experiments are conducted by filling a variety of cylindrical or conical containers with a fluid, smoothing the fluid's upper surface with a sharp edge. The containers are then quickly raised in a relatively controlled and reproducible fashion, releasing the fluid over approximately 1 s. Once the fluid achieved its maximum spreading, measurements of the final deposit are taken (a movie showing a typical dam-break experiment is available in the supplemental materials, as well as on url{https://anselmopereira.net/videos/}).

Both the initial and the final stage of a typical dam-break experiment are shown in Fig. 3. A cylindrical PVC container is filled with Mayonnaise (Mayonnaise 2 in Table 2), forming a fluid column with h_0/r_0 (Fig. $3a$). The tested Mayonnaise is mixed with a very small quantity of pink, green, and yellow dyes in order to highlight the material deformation at stoppage, after spreading over a wooden surface (Figs. $3b$, $3c$, and $3d$). As observed in Figs. $3d$, higher deformations are observed near the wood surface (pink region), while the upper part of the material tends to remains undeformed (upper part of the yellow region). We will come back to this point in the following Sections.

4 Results and Discussions

4.1 2D Bingham dam-break: comparison to Liu et al. (2016), effect of Bingham number and initial aspect ratio

First, our numerical framework is applied to 2D rectangular Bingham column collapses. The results are compared to the ones from Liu et al. (2016), and

Table 2. Details concerning the considered fluids/experiments. The yield stress values shown below were measured in a rheometer either using parallel plates or vane technique.

material	container	h_0/r_0	g [m/s^2]	ρ [kg/m^3]	τ_0 [Pa]	Bn	reference
Mayonnaise 1	cylinder	1.28-3.58	9.81	1000	200	0.1-0.4	present work
Mayonnaise 2	cylinder	0.5-2.5	9.81	1000	55	0.04-0.3	present work
Ketchup	cylinder	0.5-3.6	9.81	1000	20	0.01-0.04	present work
Carbopol	cylinder	0.96-6.5	9.81	1000	1	0.0006-0.004	present work
Carbopol	cylinder	3.43	9.81	2500	4.8-100	0.004-0.1	Pierre et al. (2013)
Carbopol	cylinder	0.8-4	9.81	1000	39	0.02-0.3	Liu et al. (2018)
red mud	cylinder	0.5	9.81	3200	40-410	0.03-0.3	Pashias et al. (1996)
zirconia	cylinder	0.5	9.81	5800	130-1050	0.04-0.4	Pashias et al. (1996)
titania	cylinder	0.5	9.81	4000	80-500	0.04-0.3	Pashias et al. (1996)
tailings (pastes)	cylinder	2	9.81	1315	18	0.1-0.6	Gao and Fourie (2015)
tailings (pastes)	cylinder/cone	0.5	9.81	4000	10-1000	0.004-0.4	Clayton et al. (2003)
cement pastes	cylinder/cone	1.92	9.81	3000	6-470	0.004-0.3	Saak et al. (2004)
pastes/suspensions	cone	1	9.81	2500	1-350	0.08-0.8	Roussel and Coussot (2005)

the same features and geometry of the flow are considered. Moreover, the regularization parameter is set to $m = 10^{-4}$, dimensionless interface thickness is set to $E = 0.003$ and minimum dimensionless mesh size is set to $l_{min} = 10^{-3}$. Lastly, both the air viscosity and the air density are constant and respectively equal to 10^{-5} Pa·s and 1 kg/m^3.

Figure 4 shows the height profile during a collapse at Bn = 0.03 and initial aspect ratio $h_0/r_0 = 1$. This figure illustrates the dimensionless deformation rate $(4a)$, the viscosity $(4b)$, both the yielded (white) and the unyielded (black) regions $(4c)$, and the mesh adaptation $(4d)$ at dimensionless time $\bar{t} = 10$ (left column) and $\bar{t} = 100$ (right column). At $\bar{t} = 10$, unyielded regions are localized at the centre of the flow, but also at the corner, which is still sharp at this stage. Thus, viscosity is maximal in these areas. Moreover, the associated mesh captures very accurately yielded and unyielded transition. During the collapse, the dead zone grows onto the fluid domain and the sharp corner vanishes completely. At $\bar{t} = 100$, the corner has nearly totally vanished. The unsheared region, located at the centre of the flow, has grown up.

A dam-break at Bn = 0.1 and initial aspect ratio $h_0/r_0 = 1$ is also performed, as shown in Fig. 5 for $\bar{t} = 10$ (left column) and $\bar{t} = 100$ (right column). The influence of Bn can be observed by comparing it with Fig. 4. At $\bar{t} = 10$, unyielded areas located both at corner and column centre are larger. Moreover, another small unyielded region appears at the front, giving a curved front shape. At $\bar{t} = 100$, the viscosity becomes very large and the flow stops. The development of the unyielded regions leads to a deformation field that is considerably less pronounced around the column centre, as previously reported by Staron et al. (2013) and experimental corroborated by the coloured layers in Fig. $3(d)$.

It is worth noting that, in Figs. 4 and 5, the size, orientation of the elements and their shape allow to resolve and capture local physical phenomena such as transition between yielded and unyielded regions. We can clearly see in Figs. 4(d) and 5(d) the appearance of different interfaces, not only between the Bingham fluid and surrounding air but also at yielded/unyielded inner interfaces.

Let us note r the instantaneous front position ($= x = y$), r_∞ the front position at the stoppage ($= x_\infty = y_\infty$), h the instantaneous column height at its symmetry plane/axis ($= z$) and h_∞ the column height at flow stop ($= z_\infty$).

In Fig. 6, the dimensionless front position $\bar{r} = r/r_0$ and the dimensionless column height $\bar{h} = h/h_0$ are plotted as a function of the dimensionless time $\bar{t}$, and are compared with the results reported by Liu et al. (2016). Figures 6(a) and 6(b) illustrate, respectively, the front position and the column height for dam-breaks with different Bingham numbers Bn and fixed initial aspect ratio $h_0/r_0 = 1$. As expected, the larger Bn, the lower the final front position and the larger the final column height. Finally, our results are in quantitative agreement with the ones presented by Liu et al. (2016).

4.2 3D computations for cylindrical columns, comparison to the 2D rectangular columns, effect of Bingham number and initial aspect ratio

The model was extended to simulate three-dimensional Bingham collapses. As for two-dimensional flows, the same values for τ_0 and k have been considered (see table 2). A mesh with minimum mesh size $l_{min} = 10^{-3}$ has been constructed. The filtering length for the Level-Set function E has been set to

three times the minimum mesh size l_{min}. Finally, the regularization parameter has been set to $m = 10^{-5}$. Both the air viscosity and the air density are constant and respectively equal to 10^{-5} Pa·s and 1 kg/m^3.

Let us first focus on the collapse dynamics for a large initial aspect ratio $h_0/r_0 = 10$ and Bingham number Bn = 0.1 in the 2D rectangular columns (Fig. 7). Contrarily to the previous case, at early times (Fig. 7, first and second column), the material mostly deforms at its bottom, while its top part is kept unyielded. The unyielded zone gets smaller during collapse (Fig. 7, third and fourth column) and then, when the potential energy starts to be no more sufficient to yield the fluid, the unyielded zones grow again, as well as a third one at the edge.

Let us consider now the 3D cylindrical columns with the same initial aspect ratio $h_0/r_0 = 10$ and Bingham number Bn = 0.1, as displayed in Fig. 8. Early times of the collapse show that a slightly smaller amount of the fluid volume is yielded, which can be explained by the additional degree of freedom (third dimension) that favours yielding (similarly, in uniaxial compression, the fluid yields for a compressive (negative) stress σ_{zz} so that $||\sigma_{zz}|| \geq 2\tau_0$ in 2D and $||\sigma_{zz}|| \geq \sqrt{3}\tau_0$ in 3D, inducing a compression rate $\dot{\gamma}_{zz} = (\tau_0 - \sigma_{zz}/2)/2k$ in 2D and $\dot{\gamma}_{zz} = (\tau_0 - \sigma_{zz}/\sqrt{3})/\sqrt{3}k$ in 3D).

Aside from the tendency to yield for slightly smaller Bingham numbers, the global collapse dynamics is very similar to the 2D case, up to the final arrest, as shown in Fig. 9.

The faster collapse dynamics occurring for 3D flows can be underlined by comparing dimensionless height at symmetry plane/axis vs. dimensionless time, as shown in Figs. 9(b) and 9(d), for various values of the Bingham number.

These plots show that the 3D collapse is systematically faster and that the final dimensionless height is lower than for the 2D case.

Comparing dimensionless front positions $\bar{r}$ vs. dimensionless time $\bar{t}$, as plotted in Figs. $9(a)$ and $9(c)$ for various Bingham numbers, we observe comparable time scales and a shorter $\bar{r}$ for the 3D case, which is explained by the extra dimension: the fluid spreads on a plane in 3D, while it spreads on a line in 2D.

Very similar conclusions can be drawn by analysing 2D rectangular and 3D cylindrical dimensionless height $\bar{h}$ vs. dimensionless time $\bar{t}$ (Figs. $10b$ and $10d$) and dimensionless front position $\bar{r}$ vs. $\bar{t}$ dimensionless time (Figs. $10a$ and $10c$) for various initial aspect ratio h_0/r_0 at a fixed Bingham number $\mathrm{Bn} = 0.1$: the 3D dynamics is systematically faster, and the final dimensionless height (resp. front position) is lower (resp. larger).

Finally, the 2D and 3D dimensionless final column height $\bar{h}_\infty$ and the relative final front position $\bar{r}_\infty - 1$ can be reasonably fitted by power-law curves within the range of initial aspect ratio $h_0/r_0 \in [1; 20]$ and various Bingham numbers from $\mathrm{Bn} = 0.01$ to $\mathrm{Bn} = 0.1$, as shown in Figs. 11. However, the fit curve directions clearly change depending on Bn, which may indicate the existence of different spreading regimes. We will come back to this point in the following Subsection.

4.3 3D computations for both cylindrical and prismatic columns, energy budget analyses, scaling laws and experimental/numerical comparisons

In this subsection, we develop theoretical analyses based on 3D numerical simulations and experiments.

The collapse evolution of cylindrical and prismatic columns is illustrated in Figs. 12(a) and 12(b), respectively, for different dimensionless instants (columns; $\bar{t}$ = 0, 10, 100, 1000) from two different views: frontal (first line) and top (second line). Despite their morphological differences, these columns exhibit the same volume and initial aspect ratio ($h_0/r_0 = 10$). In addition, their flow are associated with the same low Bingham number, Bn = 0.003. At such a low plasticity level, the yield stress plays a marginal role, which leads both the cylindrical and the prismatic column to similar and highly spread final shapes with circular transversal sections (pancake-like final shape). However, a considerably different scenario is observed at Bn = 0.3, since the spreading of both columns are partially retained by the yields-stress, as shown in Figs. 13(a) and 13(b). As a result, the upper part of the columns remains undeformed at the end of the spreading process (see sub-figures at $\bar{t} = 1000$).

Aiming to highlight the physical mechanism driving the contrasting 3D collapse scenarios stressed above, we present in Fig. 14 an energy budget analysis regarding the dam-break flow illustrated in Figs. 12 ($h_0/r_0 = 10$; Bn = 0.003) and 13 ($h_0/r_0 = 10$; Bn = 0.3). Three energy terms (made dimensionless by their sum and presented in the percentage form) are plotted as a function of the dimensionless time for the early collapse instants ($\bar{t} \leq 50$, for clarity): kinetic energy, KE (grey circles); gravitational/pressure energy, P (blue triangles); work dissipation, W (red diamonds). The latter is divided into two parts related to the viscous stress contribution W_m (orange inverted triangles) and the yield stress one W_{τ_0} (green squares). The inset plots show the energy percentage curves for longer dimensionless instants. The referred energy terms are generically denoted by Π and defined as follows:

$$KE = \frac{1}{2}\int_V \rho \parallel \mathbf{u} \parallel^2 dV \quad \text{(kinetic energy, J)}\,; \tag{30}$$

$$P = \int_V \rho g z \, dV + \int_t \int_V (\nabla p)\cdot\mathbf{u} \, dV dt \quad \text{(gravitational/pressure energy, J)}\,; \tag{31}$$

$$W = \int_t \int_V k \parallel \dot{\boldsymbol{\gamma}} \parallel^2 + \tau_0 \parallel \dot{\boldsymbol{\gamma}} \parallel dV dt \quad \text{(work dissipation, J)}\,; \tag{32}$$

$$W_m = \int_t \int_V k \parallel \dot{\boldsymbol{\gamma}} \parallel^2 dV dt \quad \text{(viscous stress contribution for } W\text{, J)}\,; \tag{33}$$

$$W_{\tau_0} = \int_t \int_V \tau_0 \parallel \dot{\boldsymbol{\gamma}} \parallel dV dt \quad \text{(yield stress contribution for } W\text{, J)}\,. \tag{34}$$

Cylindrical column results (closed symbols) are shown in the top line ($14a$ and $14b$), while prismatic column ones (opened symbols) are displayed in the bottom line ($14c$ and $14d$). Clearly, for the four cases, the kinetic energy term is negligible and then the initial gravitational energy of the columns is almost entirely dissipated by viscous effects. Such dissipation is basically driven by the viscous stress at Bn = 0.003, as illustrated by the orange inverted triangle curves in Figs. $14(a)$ and $14(c)$. However, a different mechanism is observed in Figs. $14(b)$ and $14(d)$, since at Bn = 0.3 the work dissipation is primarily related to the yield stress term. At this plasticity level, the work dissipation is pronounced and, consequently, both cylindrical and prismatic columns rapidly achieve their equilibrium state ($\bar{t} \approx 20$).

The energy curves pointed out in Fig. 14 reveal at least two different collapse scenarios. In the first one, the initial potential energy of the fluid columns ($\sim \rho g h_0^2 r_0^2$) is transferred into viscous stress work ($\sim k(U_c/h_\infty) r_\infty^3$) during the collapse. Together with volume conservation ($r_0^2 h_0 \sim r_\infty^2 h_\infty$), this yields

$$\frac{r_\infty}{r_0} \sim \left[\mathrm{Ga}\left(\frac{h_0}{r_0}\right)\right]^{\frac{1}{5}} \quad \text{and} \quad \frac{h_\infty}{h_0} \sim \left[\frac{1}{\mathrm{Ga}}\left(\frac{1}{h_0/r_0}\right)\right]^{\frac{2}{5}}, \tag{35}$$

in which Ga denotes the viscous stress based Galileo number, $\mathrm{Ga} = \frac{\rho g h_0}{k(U_c/h_0)}$.

In the second scenario, the initial potential energy is transferred into yield stress work ($\sim \tau_0 r_\infty^3$). Hence, we find through the energy conservation balance that

$$\frac{r_\infty}{r_0} \sim \left[\frac{1}{\mathrm{Bn}}\left(\frac{h_0}{r_0}\right)\right]^{\frac{1}{3}} \quad \text{and} \quad \frac{h_\infty}{h_0} \sim \left[\mathrm{Bn}\left(\frac{1}{h_0/r_0}\right)\right]^{\frac{2}{3}}, \tag{36}$$

The validity of Eqs. 35 and 36 is stressed in Figs. 15 and 16 for different cylindrical (top line) and prismatic (bottom line) Bingham columns. The former shows the final relative spreading, $(r_\infty/r_0)-1$, as a function of $(\mathrm{Ga}\ h_0/r_0)^{1/5}$ in Figs. 15(a) and 15(c) and $[1/\mathrm{Bn}\ h_0/r_0]^{1/3}$ in Figs. 15(b) and 15(d). Similarly, in the latter, the dimensionless final height h_∞/h_0 is displayed as a function of $[1/\mathrm{Ga}\ 1/(r_0/h_0)]^{2/5}$ in Figs. 16(a) and 16(c) and $[\mathrm{Bn}\ 1/(h_0/r_0)]^{2/3}$ in Figs. 16(b) and 16(d). The good agreement between these scaling (solid black curves) and the corresponding numerical results (symbols) indicates that, indeed, Eqs. 35 and 36 denote two distinguish collapse regimes: (1) the viscous regime, in which $r_\infty \sim r_0(\mathrm{Ga}\ h_0/r_0)^{1/5}$ and $h_\infty \sim h_0\,[1/\mathrm{Ga}\ 1/(h_0/r_0)]^{1/5}$; (2) the plastic regime, in which $r_\infty \sim r_0(1/\mathrm{Bn}\ h_0/r_0)^{1/3}$ and $h_\infty \sim h_0\,[\mathrm{Bn}\ 1/(h_0/r_0)]^{2/3}$. These new scaling laws are valid for both cylindrical and prismatic columns (top and bottom lines, respectively, in Figs. 15 and 16).

The different collapse regimes discussed above are represented along the common grey areas in Fig. 17, for which both the dimensionless maximum spreading, r_∞/r_0, and the dimensionless final height of the column, h_∞/h_0, are expressed as a function of the dimensionless characteristic dam-break velocity (Figs. 17a and 17b, respectively). The latter is defined as $U_c/U_{crossover}$, where $U_{crossover}$ is the crossover velocity obtained by equating Eqs. 35 and 36:

$$U_{crossover} = \frac{\tau_0^{5/3}\left(\frac{h_0}{k}\right)}{\left[\rho g h_0 \left(\frac{h_0}{r_0}\right)\right]^{2/3}} \,. \tag{37}$$

As discussed previously, for Bingham dam-breaks with negligible inertial effects, the characteristic velocity reads $U_c = (h_0/k)\,(\rho g h_0 - \tau_0)$ and, consequently, the dimensionless characteristic dam-break velocity assumes the form

$$\frac{U_c}{U_{crossover}} = \left(\frac{1}{\mathrm{Bn}} - 1\right)\left(\frac{1}{\mathrm{Bn}}\frac{h_0}{r_0}\right)^{2/3} \,. \tag{38}$$

The numerical results related to the plastic regime ($W_{\tau_0} > W_m$) appear within region I in blue ($U_c/U_{crossover} < 100$), while those linked with the viscous regimes ($W_m > W_{\tau_0}$) are placed in region III in red ($U_c/U_{crossover} > 1000$). A third and mixed regime is indicated by region II in white ($100 \leq U_c/U_{crossover} \leq 1000$), for which the viscous stress work is comparable to the yield stress one during the collapse process ($W_m \approx W_{\tau_0}$). We name it 'visco-plastic' (energy budgets for this regime are not shown in Fig. 14, for brevity). The simulations are compared with experiments either taken from existing literature or performed using tailings, mineral suspensions, Carbopol, Mayonnaise, and Ketchup for cylindrical and conical columns (see Table 2). Similar to the simulations, regardless of the initial column morphology, the experimental results are distributed along a single trajectory contained within the grey areas. In other words, experiments and simulations are in good agreement with each other, which ultimately confirms not only the validity of Eqs. 35 and 36, but also the ability of the numerical framework detailed in Section 2 to capture the physical mechanisms that drive viscoplastic dam-breaks.

Finally, in Fig. 18(a) we compare the evolution of the dimensionless front

position as a function of the dimensionless time of three 3D cylindrical dam-breaks at $h_0/r_0 = 1$ (Bn = 0.01, grey solid line; Bn = 0.03, blue dashed line; and Bn = 0.08), red dotted-line) to the correspondent cases reported by Liu et al. (2018). Once again, an excellent agreement between these simulations is observed. This is also corroborated by Fig. 18(b), where values $\bar{h}_\infty$ (magenta circles) are compared to those from Liu et al. (2018) (black asterisks) for a wide range of h_0/r_0 and Bn. As previously demonstrated, these results follow a common trajectory when plotted as function of $\left(\frac{1}{\mathrm{Bn}} - 1\right)\left(\frac{1}{\mathrm{Bn}}\frac{h_0}{r_0}\right)^{2/3}$, a collapse level that is not obtained when using the scaling explored by Liu et al. (2018) (see Fig. 11a of the referred article).

5 Concluding remarks

We investigated through 2D/3D numerical simulations, experiments and theoretical arguments the collapse of viscoplastic columns under gravity, i.e. viscoplastic dam-breaks.

The simulations were based on the development of an adaptive stabilized finite element framework able to compute efficiently free surface flows of highly viscoplastic fluids. Particularly, we focused on a Bingham yield stress fluid model. The singularities occurring at yielded/unyielded transition are smoothed with a regularization method, leading to the computation of regularized Bingham viscosity. Momentum and mass equations were solved by using a Variational MultiScale method. Additionally, the interface between viscoplastic fluid and air was captured by using the Level-Set method, and is convected by solving a transport equation coupled with the Level-Set reinitialization. The adaptive finite element framework described here was applied to 2D rectangular,

3D cylindrical, and 3D prismatic viscoplastic column collapses, multiphase complex flows with strong non-linearities and large topology changes. A wide range of initial column aspect ratio (1-20) and Bingham number (0.003-0.3) was considered.

The obtained 2D results on rectangular viscoplastic column collapses shown good agreement with literature. Additionally, new 3D simulations for both cylindrical and prismatic columns were analysed through energy budget and scaling laws based on which the collapse process was divided into three regimes: (1) viscous; (2) visco-plastic (mixed); and (3) plastic. Finally, the 3D simulations were compared to a non-exhaustive list of experiments either taken from existing literature or performed using tailings, mineral suspensions, Carbopol, Mayonnaise, and Ketchup for cylindrical and conical columns. Regardless of the initial column morphology, both numerical and experimental results collapsed into a common trajectory according to which the maximum spreading is an increasing function of the dimensionless characteristic velocity (given by the Bingham number and the initial column aspect ratio), while the final column height is a decreasing function of the latter.

The main contributions of the present work can be summarised as follows:

- A finite element framework devoted to both 2D and 3D multiphase flows with non-Newtonian materials is presented and applied to viscoplastic dam-breaks for which inertial effect are negligible;
- New 2D and 3D viscoplastic dam-break simulations for both cylindrical and prismatic columns are performed for a wide range of initial column aspect ratio (1-20) and Bingham number (0.003-0.3). New viscoplastic dam-break experiments are equally carried out using Carbopol, Mayonnaise, and

Ketchup. These new numerical/experimental results contribute to the enrichment of the literature database;

- The presented numerical results are explored through energy budget analyses, which clearly indicate the existence of three different spreading regimes: (1) a plastic regime; (2) a mixed visco-plastic regime; and (3) a viscous regime;
- The identified dam-break regimes are expressed by energy-budget-based scaling laws through which both the final front position and the final column height are predicted;
- By manipulating the new scaling laws mentioned above, it is shown that the experimental/numerical results carried out for the present work, as well as those obtained from the literature, collapse along a single trajectory according to which both the final front position and the final column height are functions of $\left(\frac{1}{\mathrm{Bn}} - 1\right)\left(\frac{1}{\mathrm{Bn}}\frac{h_0}{r_0}\right)^{2/3}$.

Finally, the good numerical/experimental agreement shown in the present work not only validates the detailed numerical framework, but also motivates us to progress towards the modelling of other non-Newtonian effects on dam-breaks (elasticity; normal stresses etc.), as well as more challenging free surface flow cases, such as the impact of non-Newtonian droplets on solid and liquid surfaces, and/or the container filling with complex fluids.

6 Acknowledgements

We would like to thank Mrs. Camila Borgo for her great help with the experiments performed here, as well as Prof. Malcolm R. Mackley (University of Cambridge) and Dr. Simon A. Butler (University of Cambridge) for some

of the rheological measurements displayed in Table 2, and Dr. P. Saramito and Dr. P.-Y. Lagrée for fruitful discussions. The authors also would like to acknowledge support from the FUI COMCEPT project and thank the PSL Research University for its support under the program 'Investissements d'Avenir' launched by the French Government and implemented by ANR with the reference ANR-10-IDEX-0001-02 PSL.

Appendix: sensitivity analysis

As exposed in Section 2, our numerical analyses are based on an adaptive stabilized finite element framework able to compute efficiently free surface flows of highly non-Newtonian materials. We choose to focus on the power-law model. Momentum and mass equations are solved by using the Variational MultiScale method coupled with a regularization technique and anisotropic mesh adaptation. A convective self-reinitialization Level-Set method is used to describe the interface evolution.

Regarding the numerical simulations presented in the present work, Fig. 19 shows a sensitivity study for the 3D Bingham dam-breaks considered in both Figs. 12 and 13: cylindrical column with $h_0/r_0 = 10$, Bn $= 0.003$ (opened red diamonds); prismatic column with $h_0/r_0 = 10$, Bn $= 0.003$ (solid red diamonds); cylindrical column with $h_0/r_0 = 10$, Bn $= 0.3$ (opened blue triangles); prismatic column with $h_0/r_0 = 10$, Bn $= 0.3$ (solid blue triangles).

Computations linking the maximum column spreading r_∞/r_0 with the number of mesh elements N per column unit volume V (N/V) are shown in Fig. $19(a)$. Each curve is constructed by keeping the Papanastasiou coefficient fixed at $n = 10^{-5}$. Clearly, r_∞/r_0 becomes mesh independent for $N/V > 15\text{x}10^6$

m^{-3} (gray regions). Furthermore, a sensitivity analysis regarding the impact of the Papanastasiou coefficient n on r_∞/r_0 is presented in Fig. 19(b) for $N/V = 25\text{x}10^6$ m^{-3}. As observed, variations of r_∞/r_0 vanish at lower values of n ($n \leq 10^{-4}$; gray region).

References

Ancey, C., 2007. Plasticity and geophysical flows: A review. Journal of Non-Newtonian Fluid Mechanics 142, 4–35.

Balmforth, N., Craster, R., Perona, P., Rust, A., Sassi, R., 2007. Viscoplastic dam breaks and the Bostwick consistometer. Journal of Non-Newtonian Fluid Mechanics 142, 63–78.

Balmforth, N., Frigaard, I., Ovarlez, G., 2014. Yielding to stress: recent developments in viscoplastic fluid mechanics. Annual Review of Fluid Mechanics 46, 121–146.

Bingham, E., 1916. An investigation of the law of plastic flows. Bulletin of the Bureau of Standards 13, 309–353.

Bingham, E., 1922. Fluidity and plasticity .

Bonito, A., Guermond, J.L., Lee, S., 2015. Numerical simulations of bouncing jets. International Journal for Numerical Methods in Fluids 80, 53–75.

Castillo, E., Codina, R., 2014. Stabilized stress-velocity-pressure finite element formulations of the Navier-Stokes problem for fluids with non-linear viscosity. Computer Methods in Applied Mechanics and Engineering 279, 554–578.

Chaparian, E., Nasouri, B., 2018. L-box - a tool for measuring the yield stress - a theoretical study. Physics of Fluids 30, 83101.

Clayton, S., Grice, T., Boger, D.V., 2003. Analysis of the slump test for on-site

yield stress measurement of mineral suspensions. International Journal of Mineral Processing 70, 3–21.

Codina, R., 1998. Comparison of some finite element methods for solving the diffusion-convection-reaction equation. Computer Methods in Applied Mechanics and Engineering 156, 185–210.

Codina, R., Principe, J., 2007. Dynamic subscales in the finite element approximation of thermally coupled incompressible flows. Intenational Journal for Numerical Methods in Fluids 2007, 707–730.

Coussot, P., 2014. Yield stress fluid flows: A review of experimental data. Journal of Non-Newtonian Fluid Mechanics 211, 31 – 49.

Cremonesi, M., Ferrara, L., Frangi, A., Perego, U., 2010. Simulation of the flow of fresh cement suspensions by a Lagrangian finite element approach. Journal of Non-Newtonian Fluid Mechanics 165, 1555–1563.

Elias, R., Coutinho, A., 2007. Stabilized edge-based finite element simulation of free-surface flows. International Journal for Numerical Methods in Fluids 54, 965–993.

Franci, A., Zhang, X., 2018. 3d bingham numerical free-surface simulation of fluids interacting with structures using the pfem. Journal of Non-Newtonian Fluid Mechanics 259, 1–15.

Gao, J., Fourie, A., 2015. Spread is better: An investigation of the mini-slump test. Minerals Engineering 71, 120–132.

Hachem, E., Feghali, S., Codina, R., Coupez, T., 2013. Immersed stress method for fluid-structure interaction using anisotropic mesh adaptation. International Journal for Numerical Methods in Engineering 94, 805–825.

Hachem, E., Rivaux, B., Kloczko, T., Digonnet, H., Coupez, T., 2010. Stabilized finite element method for incompressible flows with high Reynolds number. Journal of Computational Physics 229, 8643–8665.

Herschel, V., Bulkley, R., 1926. Konsistenz-messungen von gummi-benzollosungen. Kolloid-Z 39, 291–300.

Houzeaux, G., Vázquez, M., Aubry, R., Cela, J., 2009. A massively parallel fractional step solver for incompressible flows. Journal of Computational Physics 228, 6316 – 6332.

Huang, X., Garcia, M.H., 1998. A Herschel-Buckley model for mud flow down a slope. Journal of Fluid Mechanics 374, 305–333.

Hugues, T., 1995. Multiscale phenomena: Green's functions, the Dirichlet-to-Neumann formulation, subgrid scale models, bubbles and the origin of stabilized methods. Computer Methods in Applied Mechanics and Engineering 127, 387–401.

Hugues, T., Feijoo, G., Mazzei, L., Quincy, J., 1998. The variational multiscale method - a paradigm for computational mechanics. Computer Methods in Applied Mechanics and Engineering 166, 3–24.

Hugues, T., Scovazzi, G., Bochev, P., Buffa, A., 2006. A multiscale discontinuous Galerkin method with the computational structure of a continuous Galerkin method. Computer Methods in Applied Mechanics and Engineering 195, 19–22.

Ji, H., Chopp, D., Dolbow, J., 2002. A hybrid extended finite element/level set method for modeling phase transformations. International Journal for Numerical Methods in Engineering 54, 1209–1233.

Khalloufi, M., Mesri, Y., Valette, R., Massoni, E., Hachem, E., 2016. High fidelity anisotropic adaptive variational multiscale method for multiphase flows with surface tension. Computer Methods in Applied Mechanics and Engineering 307, 44–67.

Lins, E., Elias, R., Rochinha, F., Coutinho, A., 2010. Residual-based variational multiscale simulation of free surface flows. Computational Mechanics

46, 545–557.

Liu, Y., Balmforth, N., Hormozi, S., 2018. Axisymmetric viscoplastic dambreaks and the slump test. Journal of Non-Newtonian Fluid Mechanics 258, 45–57.

Liu, Y., Balmforth, N., Hormozi, S., Hewitt, D., 2016. Two-dimensional viscoplastic dambreaks. Journal of Non-Newtonian Fluid Mechanics 238, 65–79.

Matson, G., Hogg, A., 2007. Two-dimensional dam break flows of Herschel–Bulkley fluids: The approach to the arrested state. Journal of Non-Newtonian Fluid Mechanics 142, 79–94.

Modolo, A., Loureiro, B., Soares, E., Thompson, R., 2019. Influence of the plastic number on the evolution of a yield stress material subjected to a dam break. Journal of Applied Fluid Mechanics 12, 1967–1978.

Nakshatrala, K., Turner, D., Hjelmstad, K., Masud, A., 2006. A stabilized mixed finite element method for Darcy flow based on a multiscale decomposition of the solution. Computer Methods in Applied Mechanics and Engineering 195, 33–36.

Nguyen, T., Roussel, N., Coussot, P., 2006. Correlation between L-box test and rheological parameters of a homogeneous yield stress fluid. Cement and Concrete Research 36, 1789–1796.

Nikitin, K.D., Olshanskii, M.A., Terekhov, K.M., Vassilevskiv, Y.V., 2011. A numerical method for the simulation of free surface flows of viscoplastic fluid in 3d. Journal of Computational Mathematics 29, 605–622.

Olsson, E., Kreiss, G., 2005. A conservative level set method for two phase flow. Journal of Computational Physics 210, 225–246.

Osher, S., Fedkiw, R., 2001. Level- set methods: An overview and some recent results. Journal of Computational Physics 169, 463–502.

Osher, S., Sethian, J.A., 1988. Fronts propagating with curvature dependent speed: algorithms based on Hamilton-Jacobi formulations. Journal of Computational Physics 79, 12–49.

Papanastasiou, T., 1987. Flows of materials with yield. Journal of Rheology 31, 385–404.

Pashias, N., Boger, D., Summers, J., Glenister, D., 1996. A fifty cent rheometer for yield stress measurement. Journal of Rheology 40, 1179–1189.

Pereira, A., Hachem, E., Valette, R., 2020. Inertia-dominated coiling instabilities of power-law fluids. Journal of Non-Newtonian Fluid Mechanics 282, 104321.

Pereira, A., Larcher, A., Hachem, E., Valette, R., 2019. Capillary, viscous, and geometrical effects on the buckling of power-law fluid filaments under compression stresses. Computers & Fluids 190, 514–519.

Pierre, A., Lanos, C., Estellé, P., 2013. Extension of spread-slump formulae for yield stress evaluation. Applied Rheology 23 (63849), 1–9.

Rao, M.A., Bourne, M., 1977. Analysis of the plastometer and correlation of Bostwick consistometer data. Journal of Food Science 42, 261–264.

Riber, S., Valette, R., Mesri, Y., Hachem, E., 2016. Adaptive variational multiscale method for Bingham flows. Computers and Fluids 138, 51–60.

Roquet, N., Saramito, P., 2003. An adaptive finite element method for Bingham fluid flows around a cylinder. Computer methods in applied mechanics and engineering 192, 3317–3341.

Roussel, N., 2007. The LCPC BOX: a cheap and simple technique for yield stress measurements of scc. Materials and Structures 40, 889–896.

Roussel, N., Coussot, P., 2005. Fifty-cent rheometer for yield stress measurements: from slump to spreading flow. International Journal of Mineral Processing 43, 705–718.

Saak, A., Jennings, H., Shah, S., 2004. A generalized approach for the determination of yield stress by slump and slump flow. Cement and Concrete Research 34, 363–371.

Saramito, P., Wachs, A., 2017. Progress in numerical simulation of yield stress fluid flows. Rheologica Acta 56, 211–230.

Schowalter, W., Christensen, G., 1998. Toward a rationalization of the slump test for fresh concrete: Comparisons of calculations and experiments. Journal of Rheology 42, 865–870.

Scovazzi, G., 2012. Lagrangian shock hydrodynamics on tetrahedral meshed: a stable and accurate variational multiscale approach. Journal of Computational Physics 231, 8029–8069.

Staron, L., Lagrée, P.Y., Ray, P., Popinet, S., 2013. Scaling laws for the slumping of a Bingham plastic fluid. Journal of Rheology 57, 1265–1280.

Thompson, R., Sica, L., de Souza Mendes, P., 2018. The yield stress tensor. Journal of Non-Newtonian Fluid Mechanics 261, 211–219.

Thompson, R.L., Soares, E.J., 2016. Viscoplastic dimensionless numbers. Journal of Non-Newtonian Fluid Mechanics 238, 57–64.

Valette, R., Hachem, E., Khalloufi, M., Pereira, A., Mackley, M., Butler, S., 2019. The effect of viscosity, yield stress, and surface tension on the deformation and breakup profiles of fluid filaments stretched at very high velocities. Journal of Non-Newtonian Fluid Mechanics 263, 130–139.

Venkatesan, J., Sankar, D.S., Hemalatha, K., Yazariah, Y., 2013. Mathematical analysis of Casson fluid model for blood rheology in stenosed narrow arteries. Journal of Applied Mathematics 2013, 583809.

Vola, D., Babik, F., Latche, J.C., 2004. On a numerical strategy to compute gravity currents of non-Newtonian fluids. Journal of Computational Physics 201, 397–420.

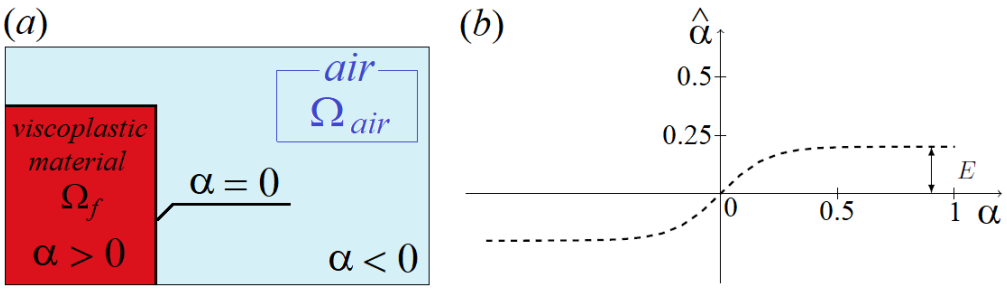

Fig. 1. (a) Computation of the initial signed distance function α in the initialization step of a column collapse computation. (b) Filtering curve for the Level-Set function.

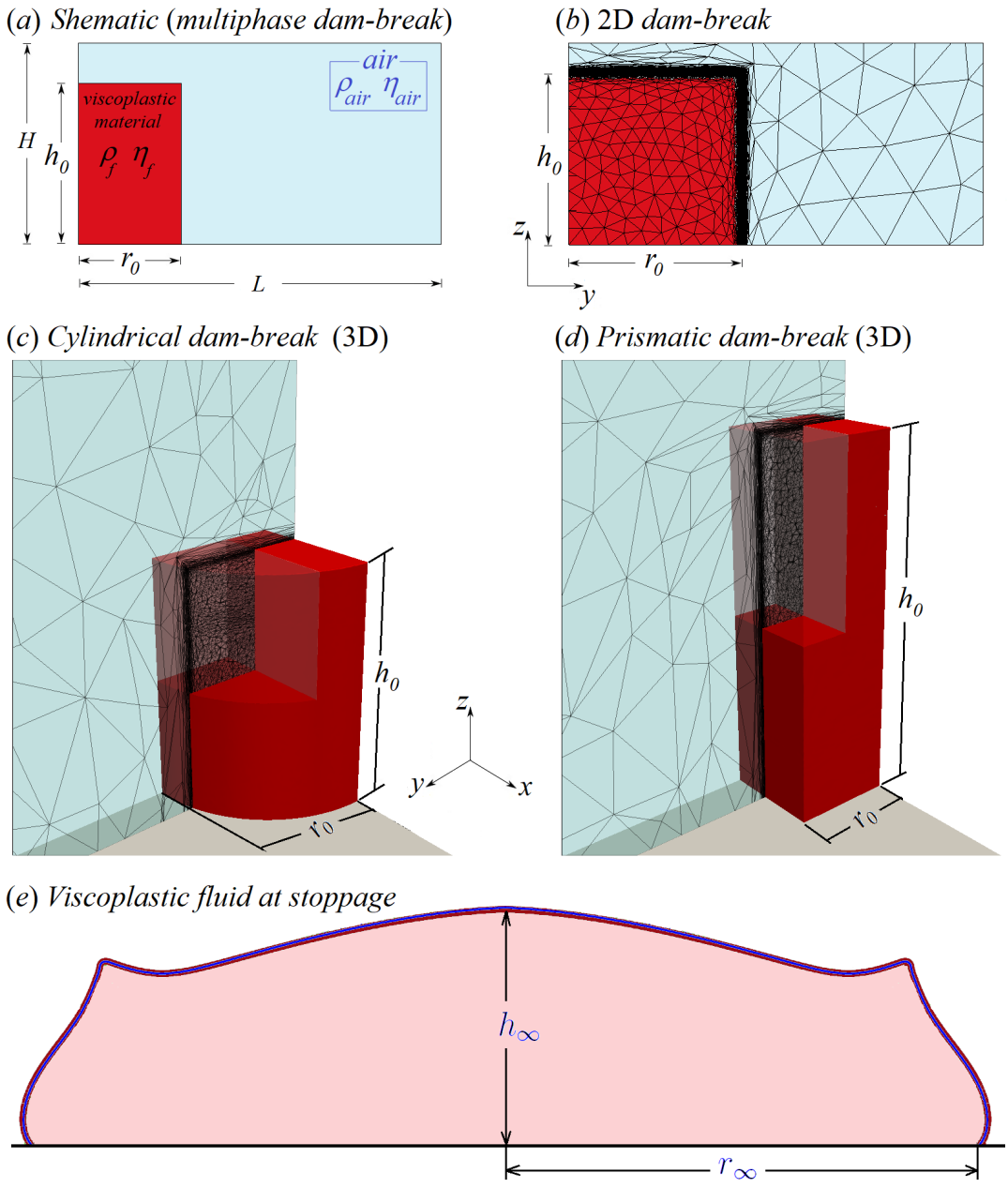

Fig. 2. (a) Schematic: multiphase dam-break flow (Bingham fluid in red; air in blue). (b) Initialization of a 2D Bingham dam-break. (c) Initialization of a 3D cylindrical Bingham dam-break. (d) Initialization of a 3D prismatic Bingham dam-break. (e) Schematic: Bingham fluid at stoppage. Black lines in the blue $y-z$ planes illustrates the mesh.

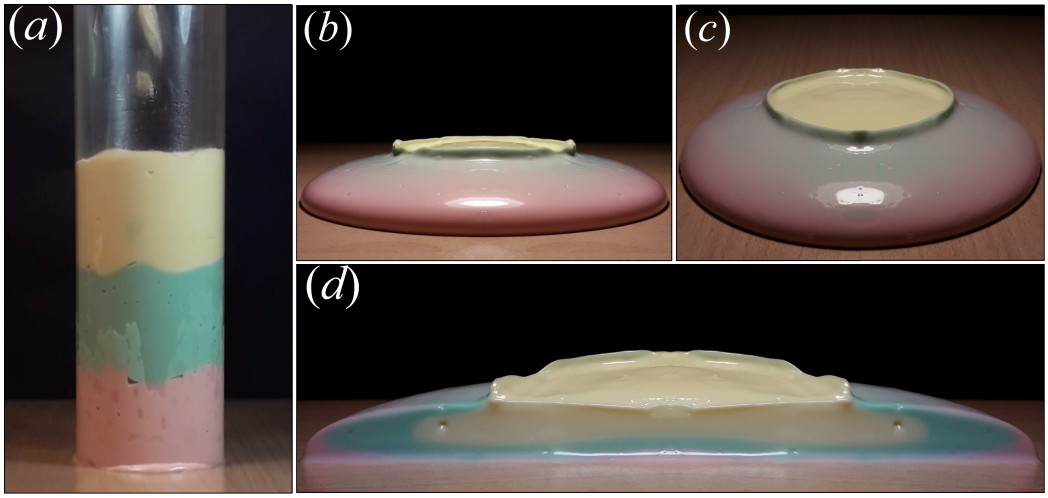

Fig. 3. (a) A cylindrical PVC container is filled with Mayonnaise (Mayonnaise 2 in Table 2), forming a fluid column with h_0/r_0. The tested Mayonnaise is mixed with a very small quantity of pink, green, and yellow dyes in order to highlight the material deformation at stoppage, after spreading over a wooden surface. The final shape of the Mayonnaise is shown in (b) and (c), while its inner deformations are illustrated by the coloured layers in (d).

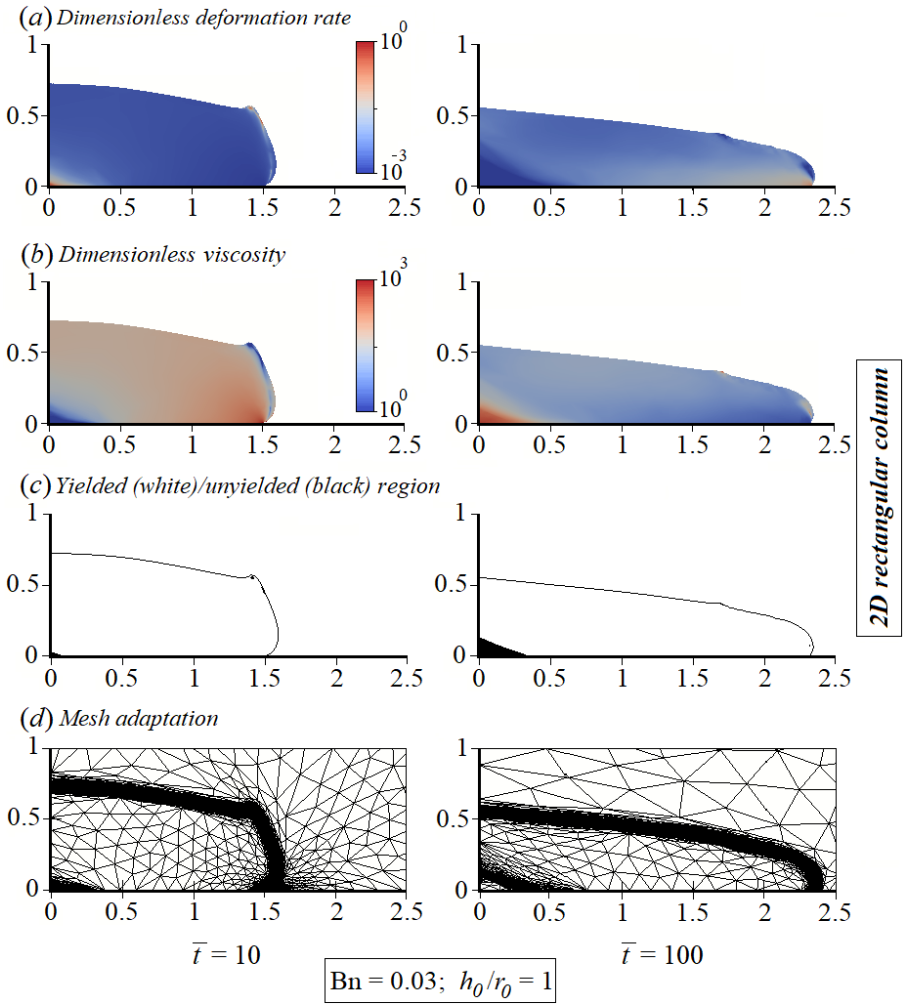

Fig. 4. 2D rectangular dam-break of a Bingham fluid with $h_0/r_0 = 1$, Bn $= 0.03$ at $\bar{t} = 10$ (left column) and $\bar{t} = 100$ (right column): (a) dimensionless deformation rate; (b) dimensionless viscosity; (c) yielded (white) and unyielded (black) regions; (d) mesh adaptation.

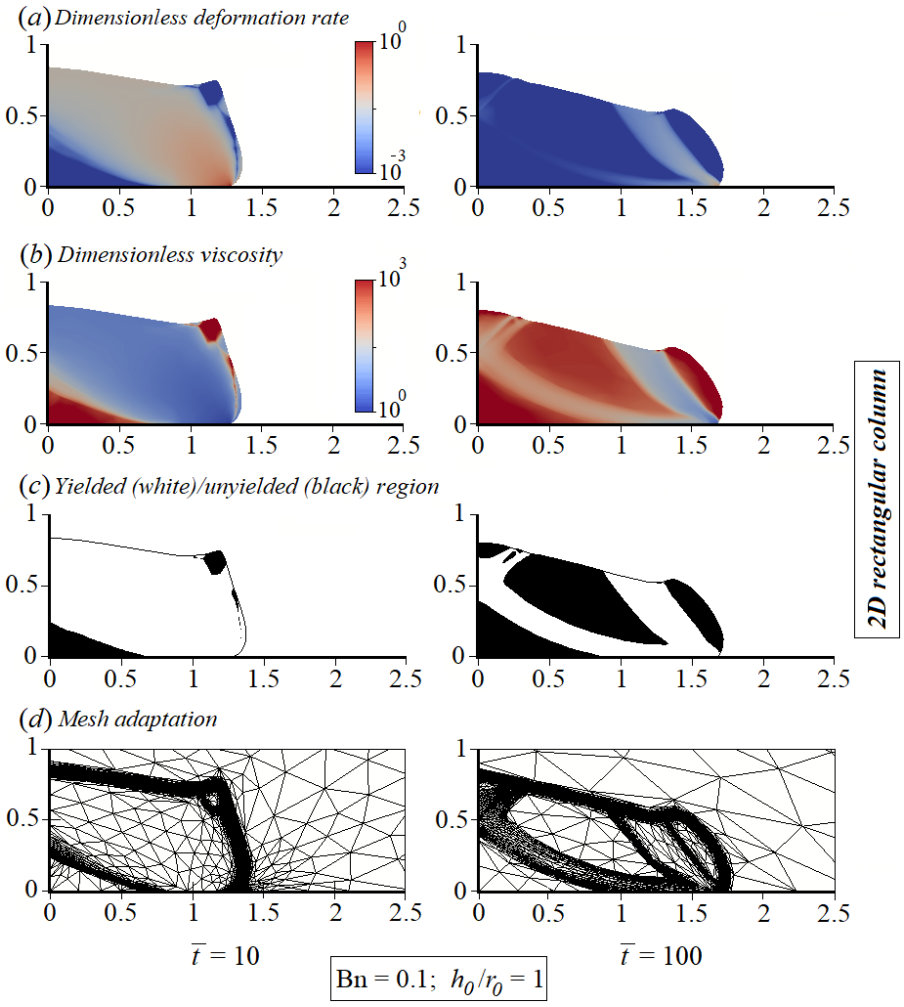

Fig. 5. 2D rectangular dam-break of a Bingham fluid at $h_0/r_0 = 1$ and Bn = 0.1. Two dimensionless instants are considered: $\bar{t} = 10$ (left column) and $\bar{t} = 100$ (right column). (a) dimensionless deformation rate. (b) dimensionless viscosity. (c) yielded (white) and unyielded (black) regions. (d) mesh adaptation.

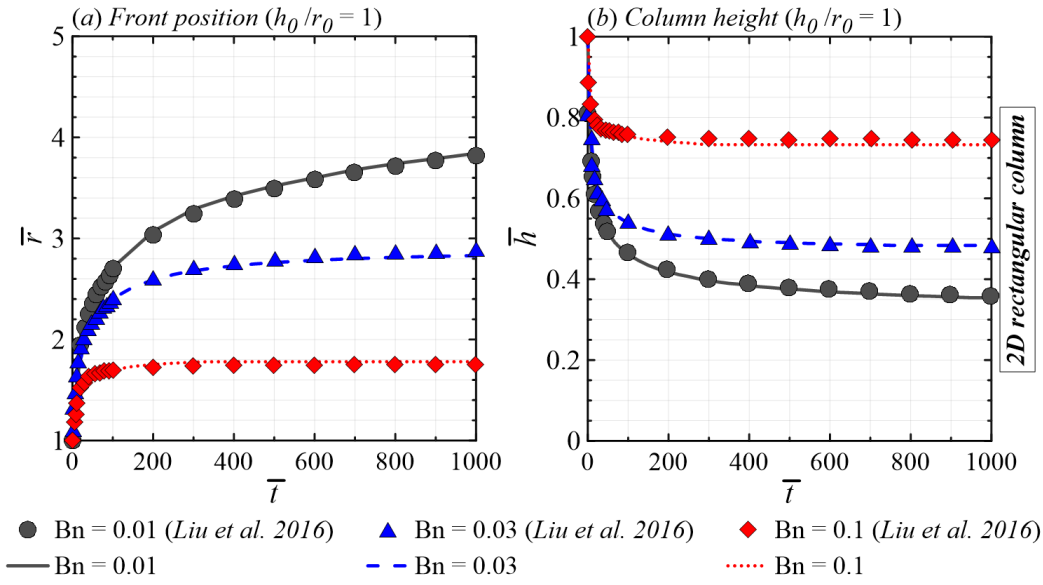

Fig. 6. 2D rectangular Bingham dam-breaks as a function of dimensionless time for different Bn (lines) and comparisons with Liu et al. (2016) (symbols) for an initial aspect ratio $h_0/r_0 = 1$: (a) dimensionless front position; (b) dimensionless column height at symmetry plane.

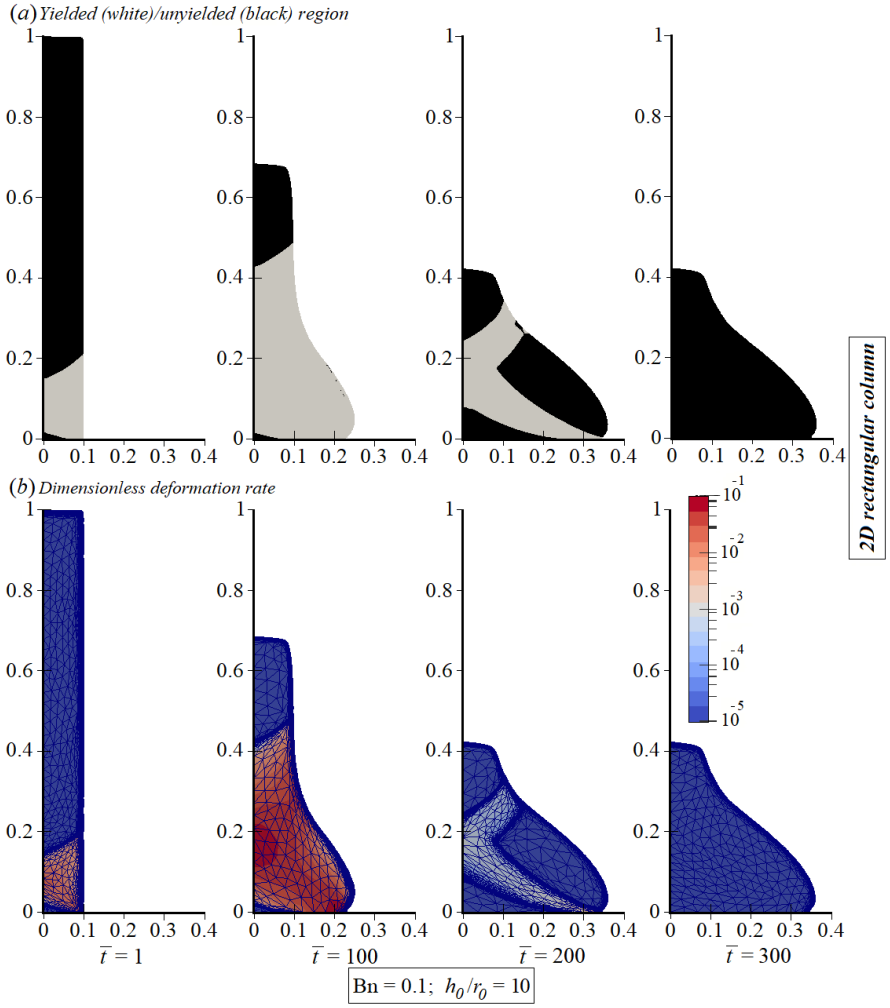

Fig. 7. 2D rectangular dam-break of a Bingham fluid at $h_0/r_0 = 10$ and Bn $= 0.1$: Four dimensionless instant are considered: $\bar{t} = 1$ (first column), $\bar{t} = 100$ (second column), $\bar{t} = 200$ (third column) and $\bar{t} = 300$ (fourth column). (a) yielded (white) and unyielded (black) regions. (b) dimensionless deformation rate.

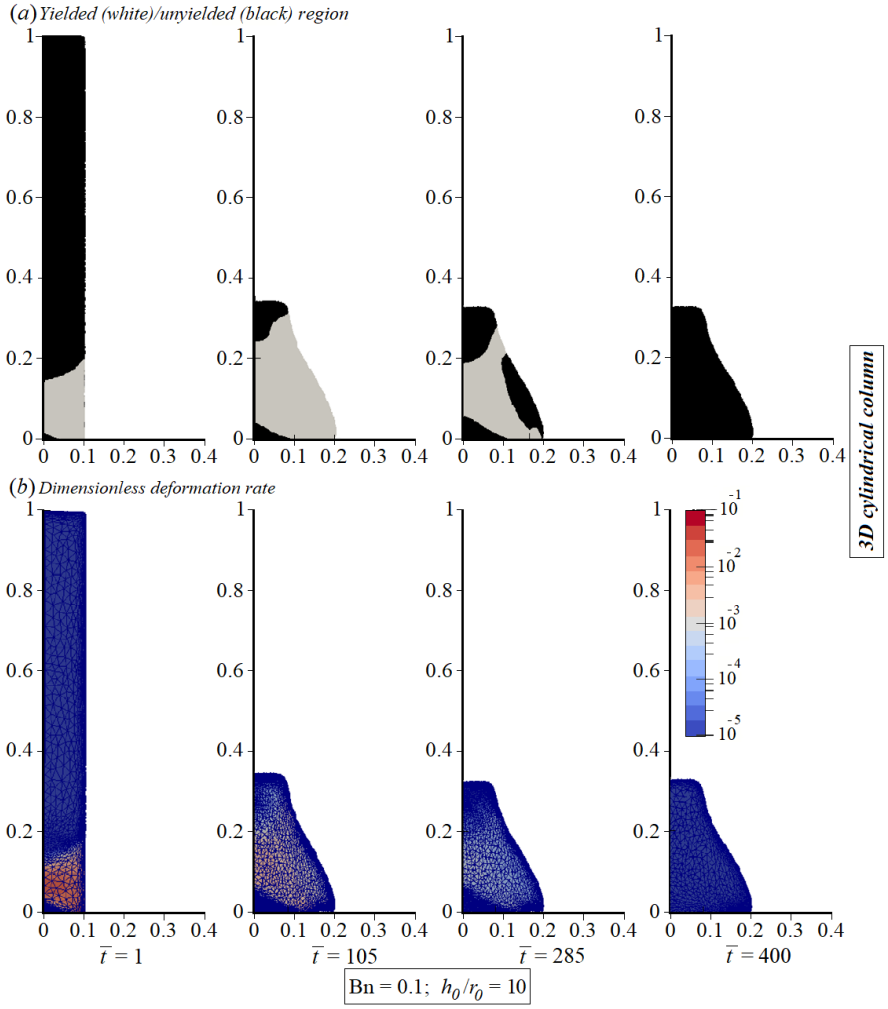

Fig. 8. 3D cylindrical dam-break of a Bingham fluid at $h_0/r_0 = 10$ and Bn = 0.1: Four dimensionless instants are considered: $\bar{t} = 1$ (first column), $\bar{t} = 105$ (second column), $\bar{t} = 285$ (third column) and $\bar{t} = 400$ (fourth column). (a) yielded (white) and unyielded (black) regions. (b) dimensionless deformation rate.

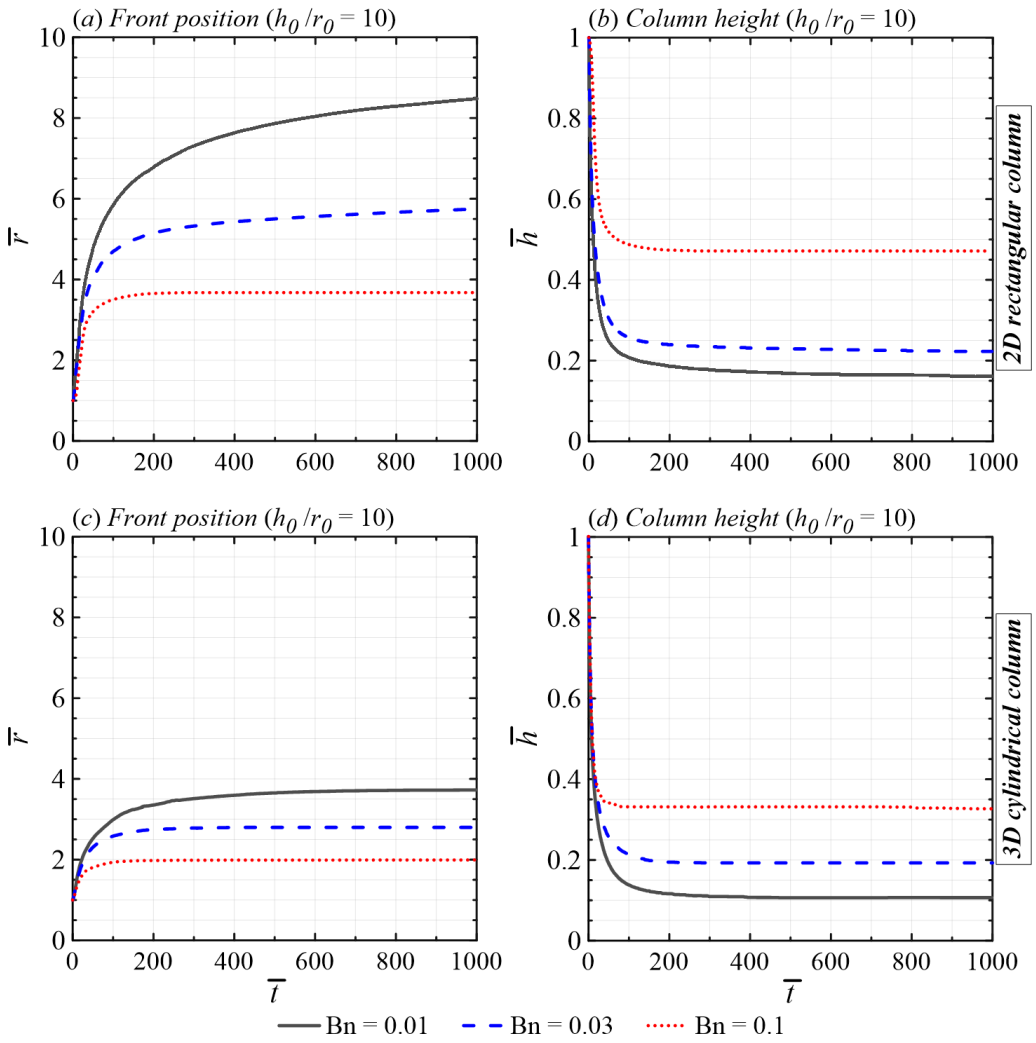

Fig. 9. 2D rectangular (a and b) and 3D cylindrical (c and d) Bingham dam-breaks for different Bn at $h_0/r_0 = 10$: (a and c) dimensionless front position; (b and d) dimensionless column height.

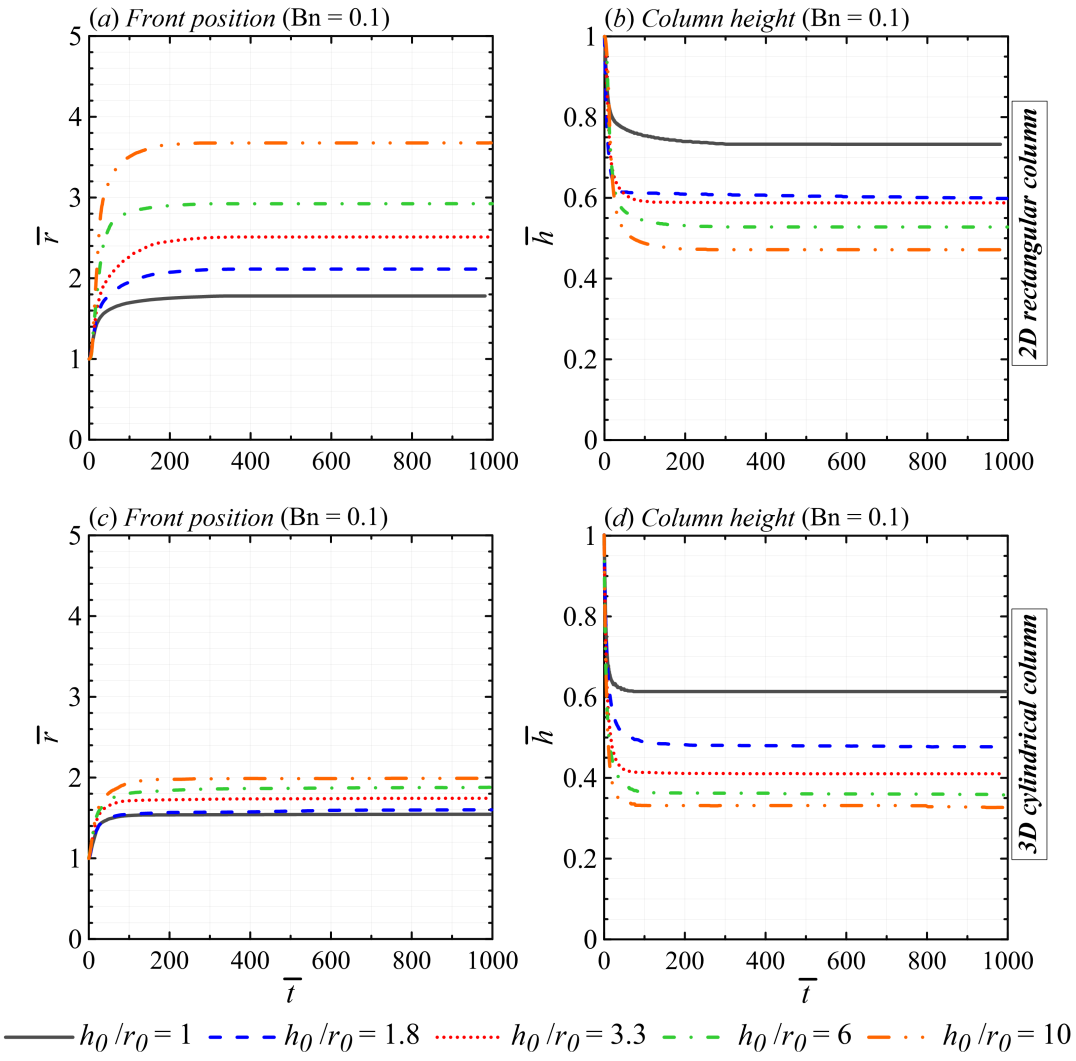

Fig. 10. 2D rectangular (a and b) and 3D cylindrical (c and d) Bingham dam-breaks for different h_0/r_0 at Bn = 0.1: (a and c) dimensionless front position as a function of $\bar{t}$; (b and d) dimensionless height as a function of $\bar{t}$.

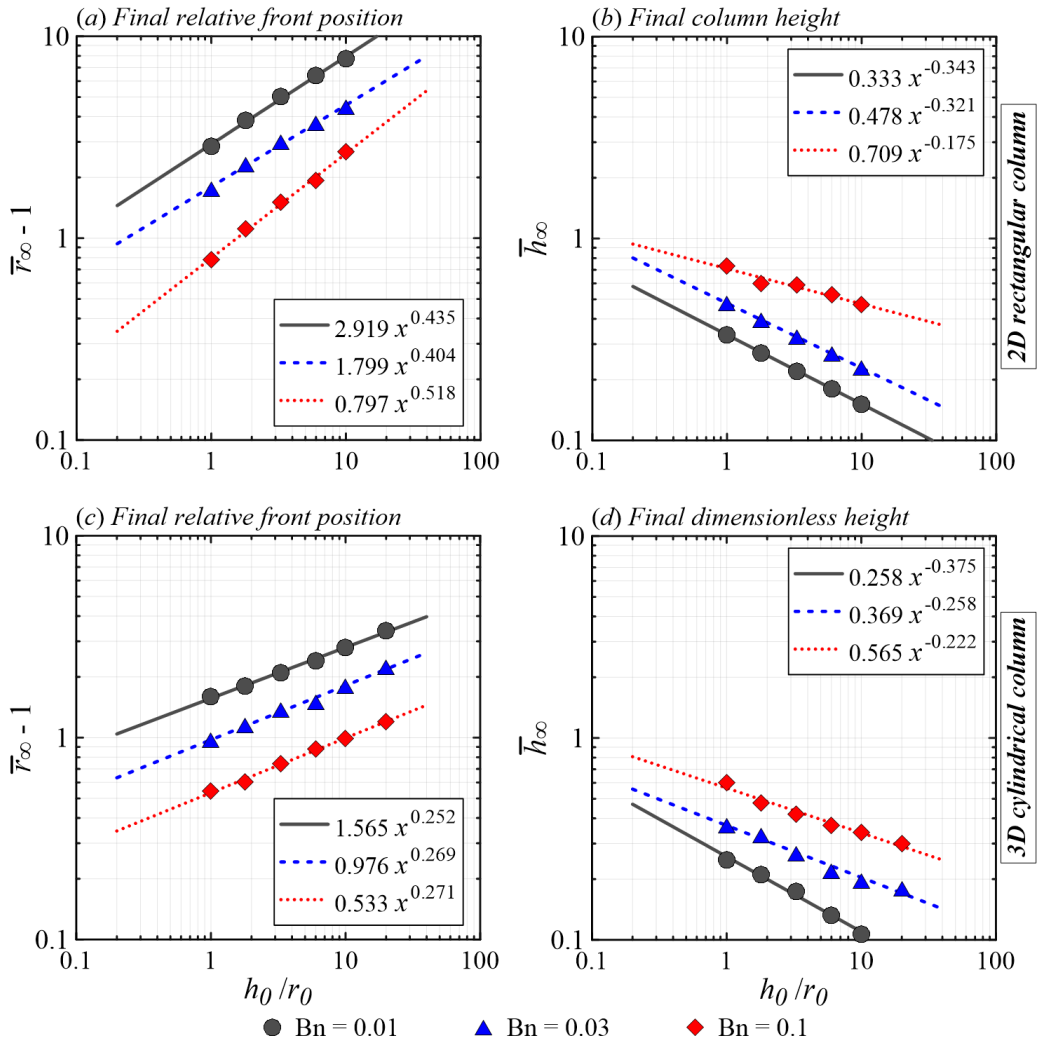

Fig. 11. Both final relative front position (a) and final column height (b) as a function of h_0/r_0 for 2D rectangular columns. Both final relative front position (c) and final column height (d) as a function of h_0/r_0 for 3D cylindrical columns. Three Bingham number are considered: Bn = 0.01 (grey circles); Bn = 0.03 (blue triangle); and Bn = 0.1 (red diamonds).

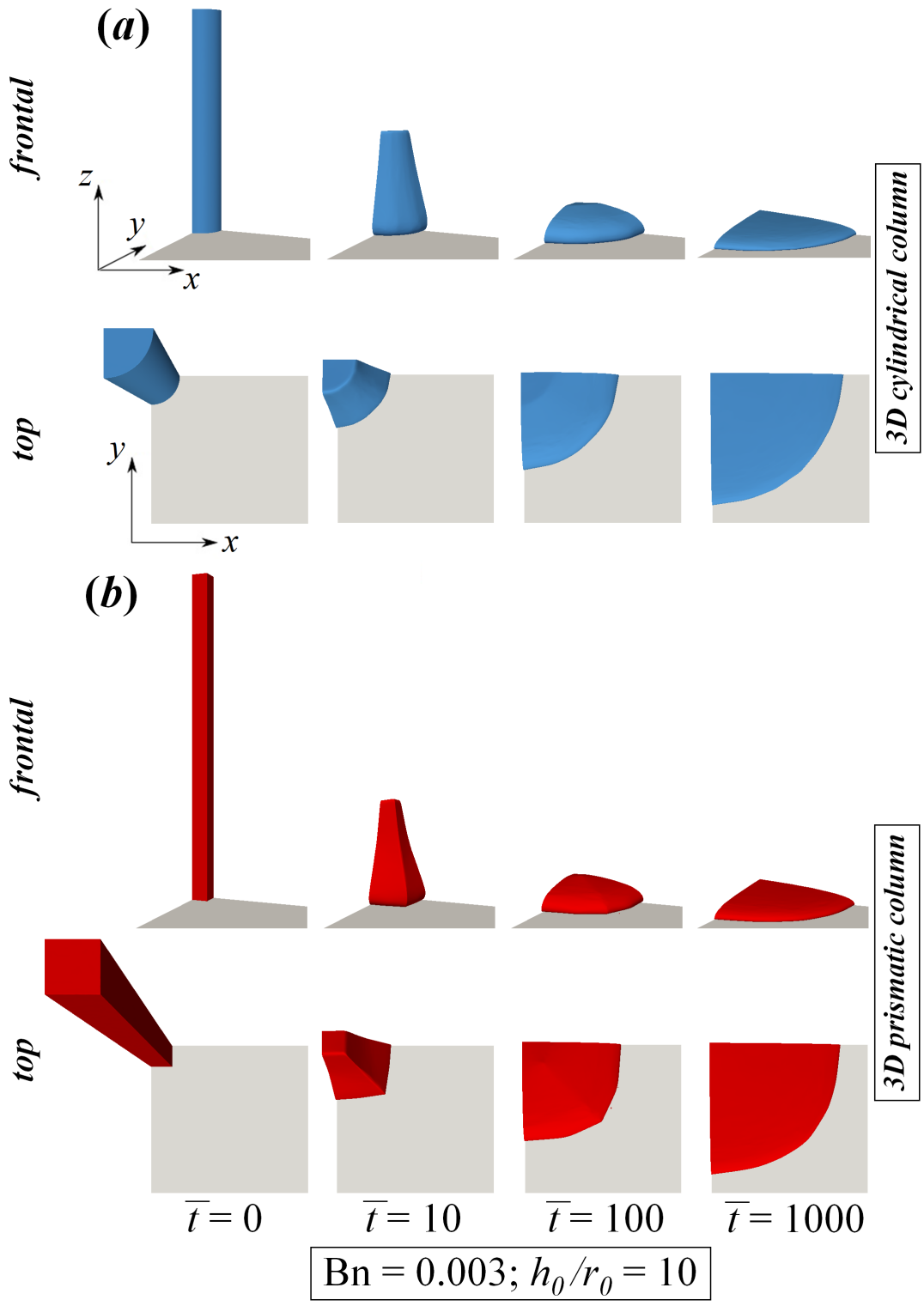

Fig. 12. Collapse evolution of 3D cylindrical (a) and 3D prismatic (b) columns at Bn = 0.003 and $h_0/r_0 = 10$ for different dimensionless instants (columns; $\bar{t} = 0$, 10, 100, 1000) from two different views: frontal (first line) and top (second line). A movie concerning these flow cases is available in the supplemental materials, as well as on url{https://anselmopereira.net/videos/}.

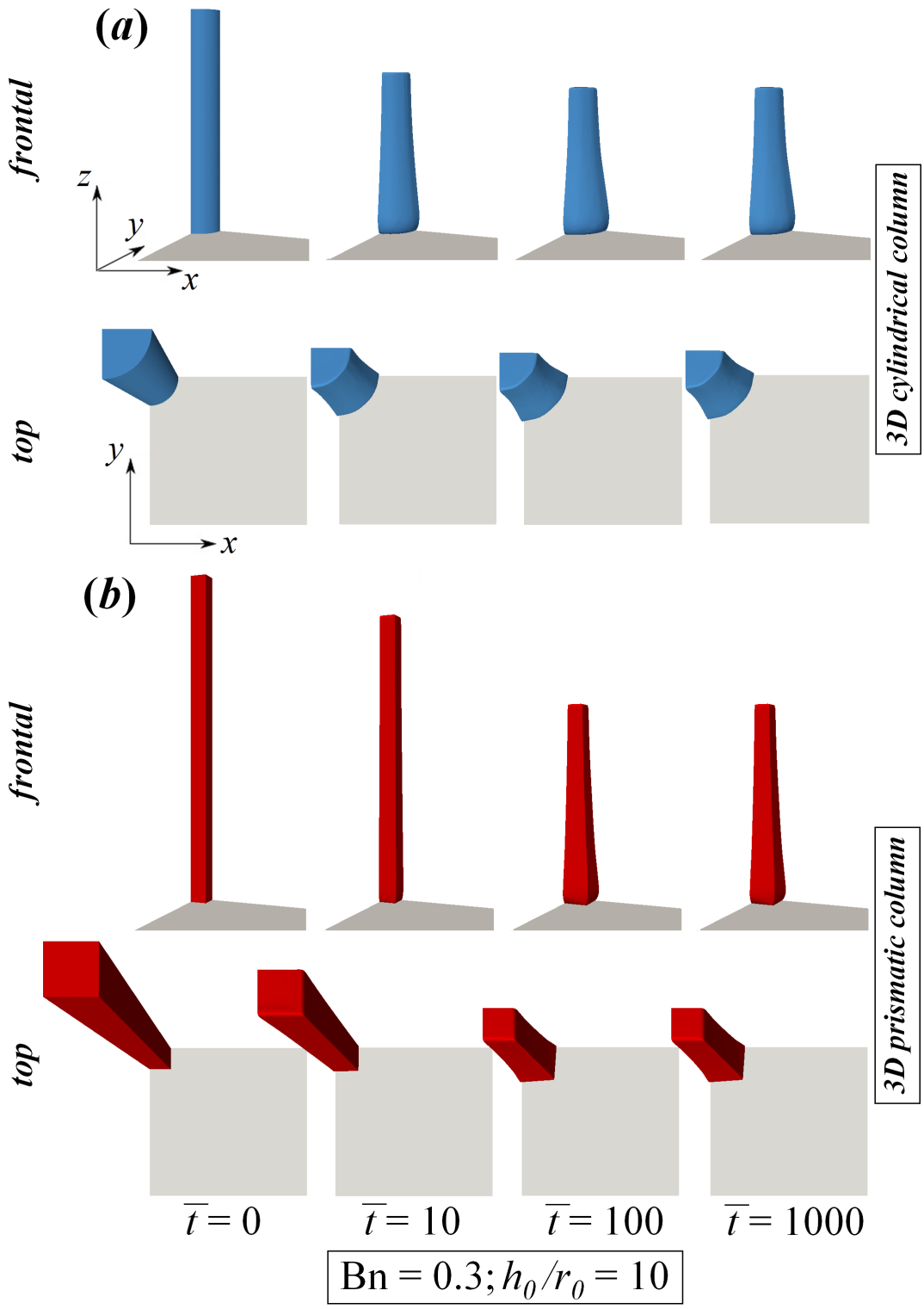

Fig. 13. Collapse evolution of 3D cylindrical (a) and 3D prismatic (b) columns at Bn = 0.3 and $h_0/r_0 = 10$ for different dimensionless instants (columns; $\bar{t} = 0$, 10, 100, 1000) from two different views: frontal (first line) and top (second line). A movie concerning these flow cases is available in the supplemental materials, as well as on url{https://anselmopereira.net/videos/}.

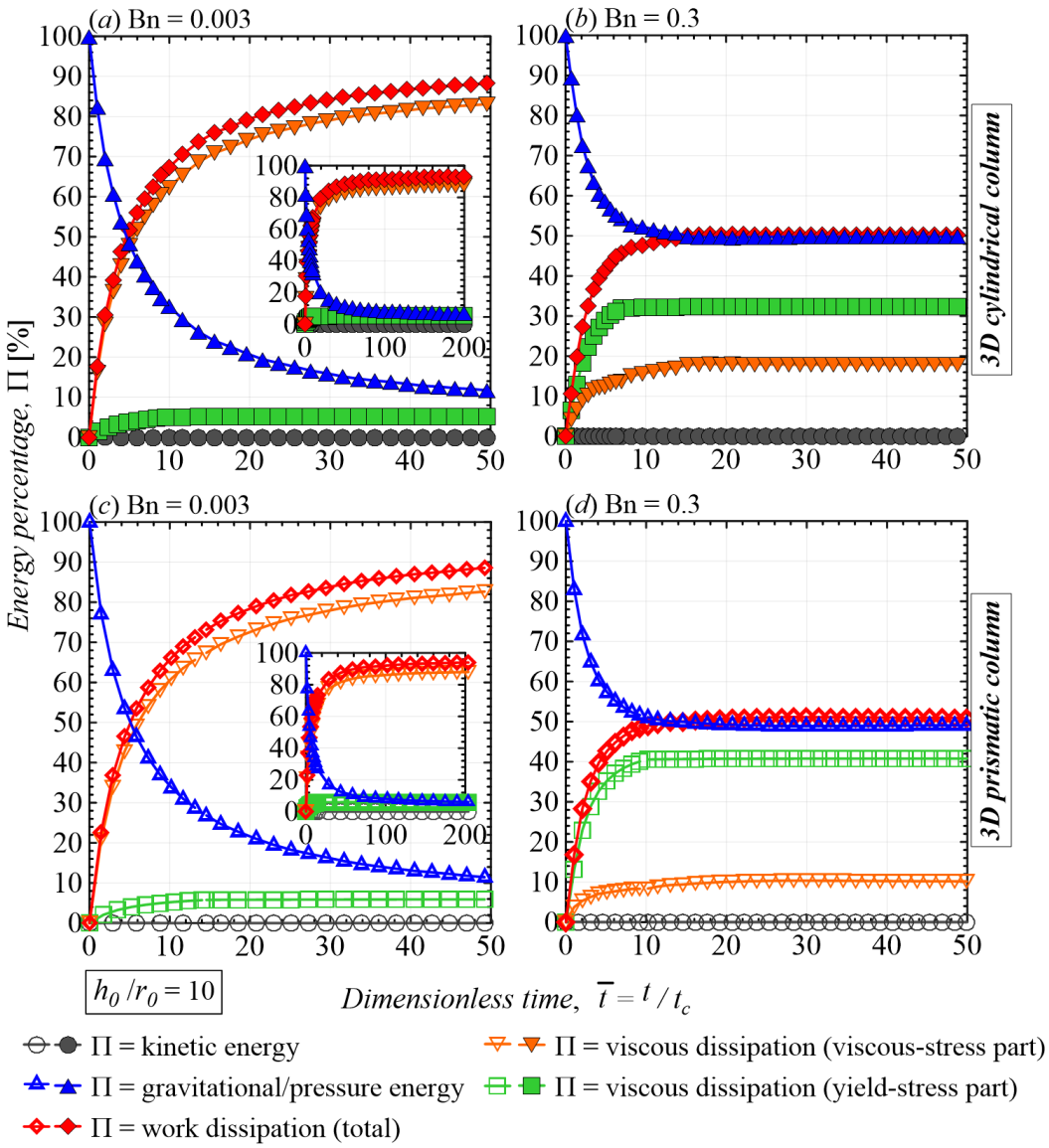

Fig. 14. Energy budget analysis for four 3D Bingham dam-breaks at $h_0/r_0 = 10$: (a) 3D cylindrical column at Bn = 0.003; (b) 3D cylindrical column at Bn = 0.3; (c) 3D prismatic column at Bn = 0.003; (d) 3D prismatic column at Bn = 0.3. Three energy terms (generically denoted by Π and made dimensionless by their sum and presented in the percentage form) are plotted as a function of the dimensionless time for the early collapse instants: kinetic energy (grey circles); gravitational/pressure energy (blue triangles); work dissipation (red diamonds). The latter is divided into two parts related to the viscous stress contribution (orange inverted triangles) and the yield stress one (green squares). The inset plots show the energy percentage curves for longer dimensionless instants.

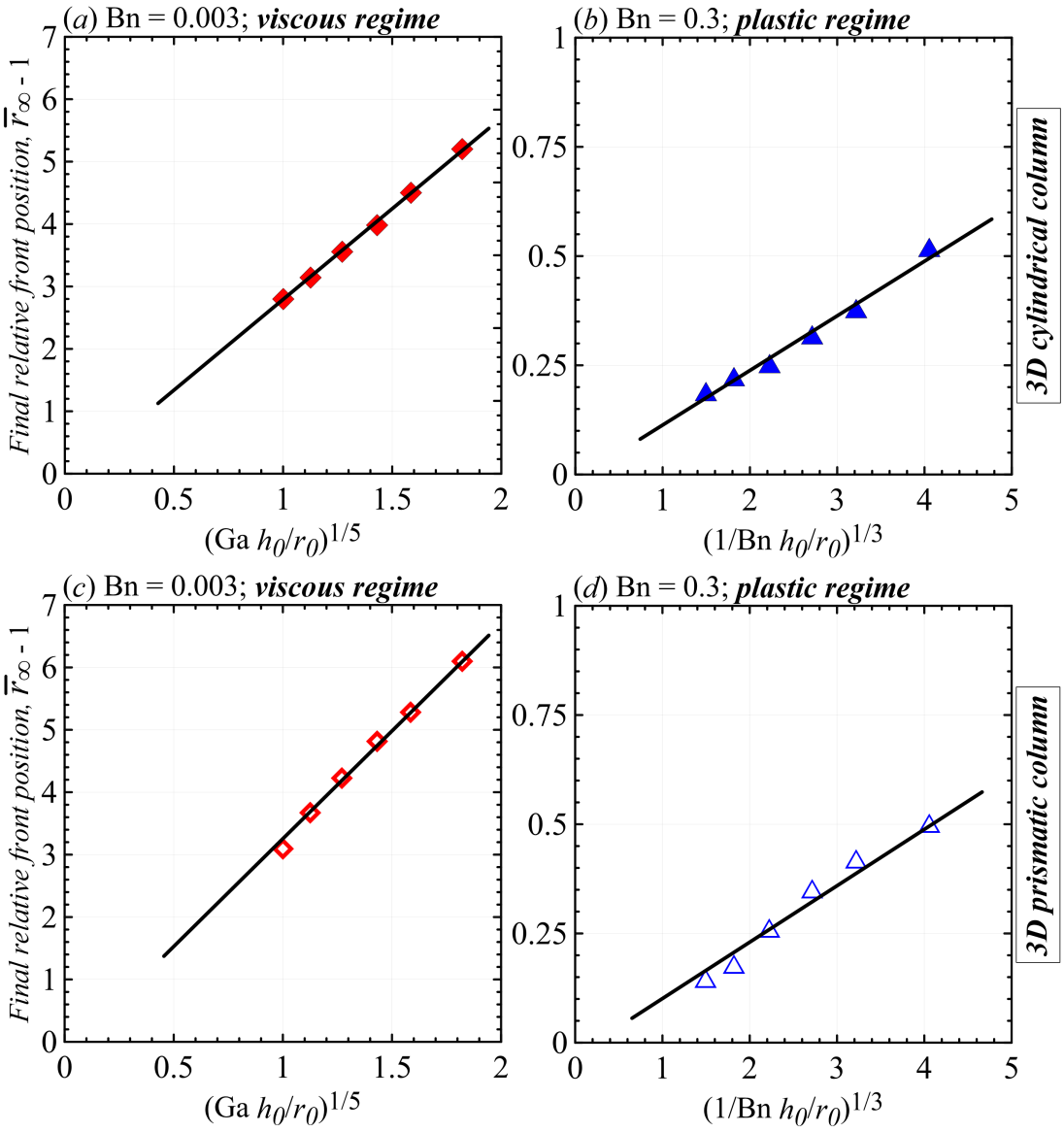

Fig. 15. Final relative front position, $(r_\infty/r_0) - 1$, as a function of (Ga $h_0/r_0)^{1/5}$ and $(1/\mathrm{Bn}\ h_0/r_0)^{1/3}$ for both 3D cylindrical (first line) and 3D prismatic (second line) columns. (a and c) Bn = 0.003. (b and d) Bn = 0.3.

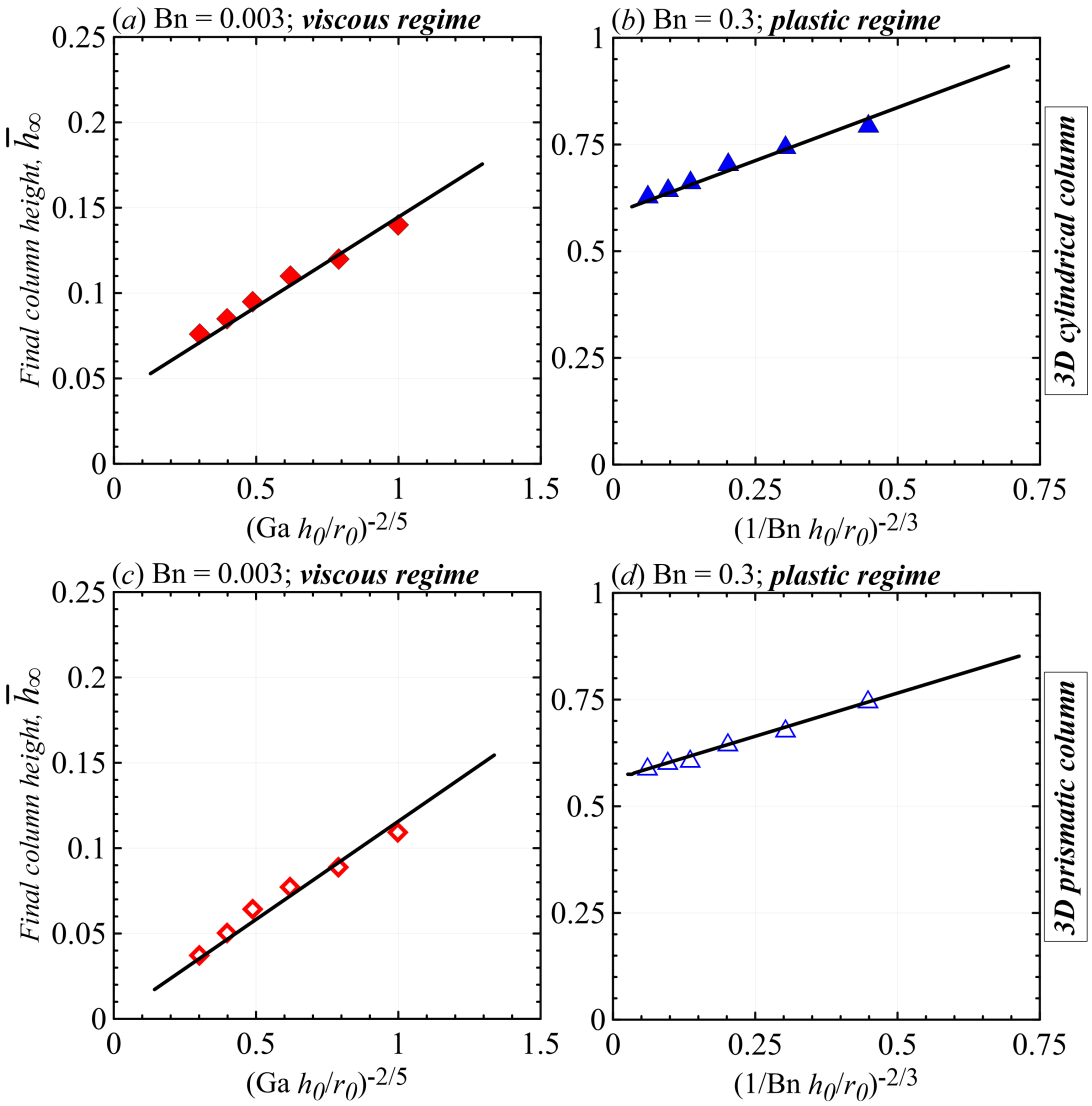

Fig. 16. Final column height, h_∞/h_0, as a function of (Ga $h_0/r_0)^{-2/5}$ and (1/Bn $h_0/r_0)^{-2/3}$ for both 3D cylindrical (firs line) and 3D prismatic (second line) columns. (a and c) Bn = 0.003. (b and d) Bn = 0.3.

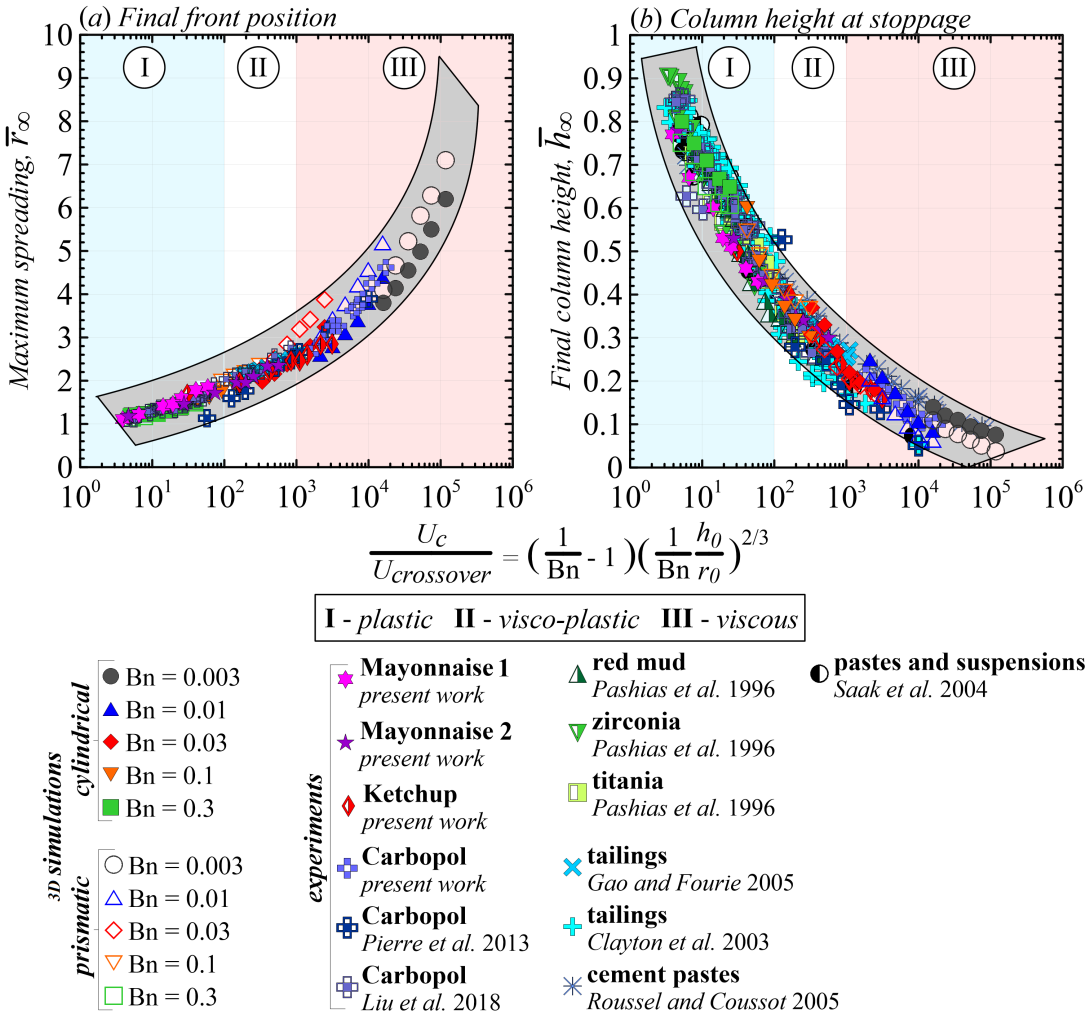

Fig. 17. The dimensionless maximum spreading r_∞/r_0 (a) and the dimensionless final height of the column h_∞/h_0 (b) are expressed as a function of the dimensionless characteristic dam-break velocity $U_c/U_{crossover}$. The numerical results related to the plastic regime appear within region I in blue ($U_c/U_{crossover} < 100$), while those linked with the viscous regimes are placed in region III in red ($U_c/U_{crossover} > 1000$). A mixed regime called here 'visco-plastic' is indicated by region II in white ($100 \leq U_c/U_{crossover} \leq 1000$). The simulations are compared with experiments either taken from existing literature or performed using tailings, mineral suspensions, Carbopol, Mayonnaise, and Ketchup for cylindrical and conical columns (see Table 2).

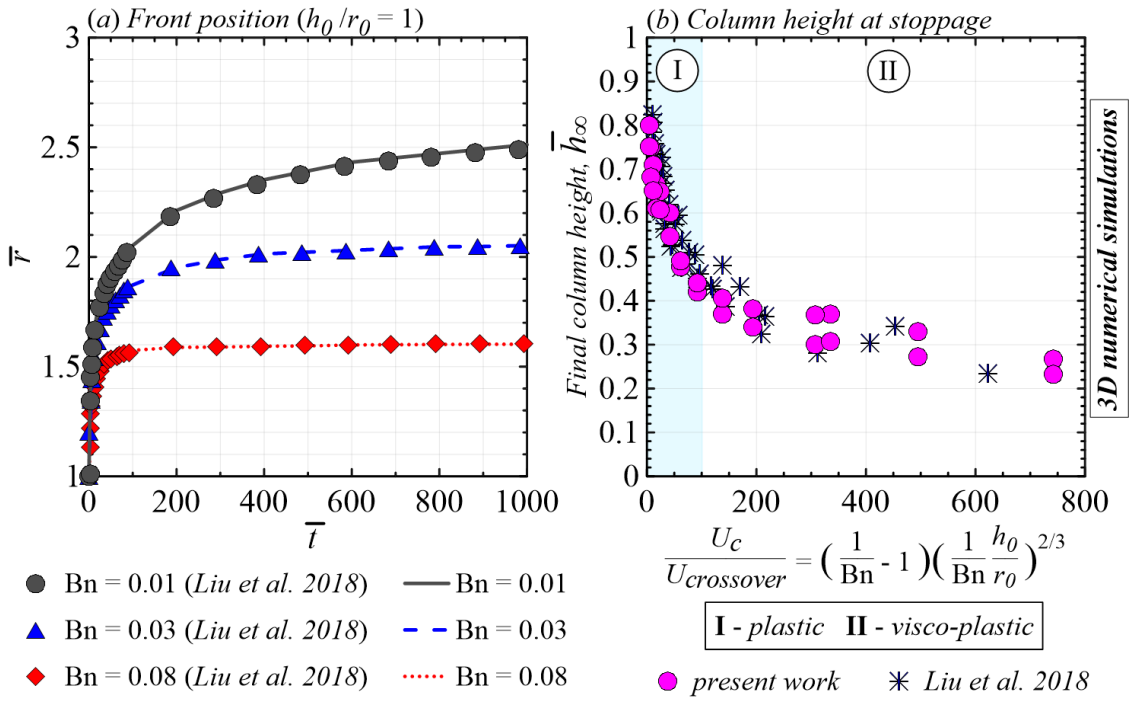

Fig. 18. (a) 3D cylindrical Bingham dam-breaks: front position as a function of the dimensionless time for different Bn (lines) and comparisons with Liu et al. (2018) (symbols) for an initial aspect ratio $h_0/r_0 = 1$. (b) Dimensionless final height of the column as a function of the dimensionless characteristic dam-break velocity $U_c/U_{crossover}$. Our numerical results (magenta circles) are compared with those from Liu et al. (2018) (black asterisks).

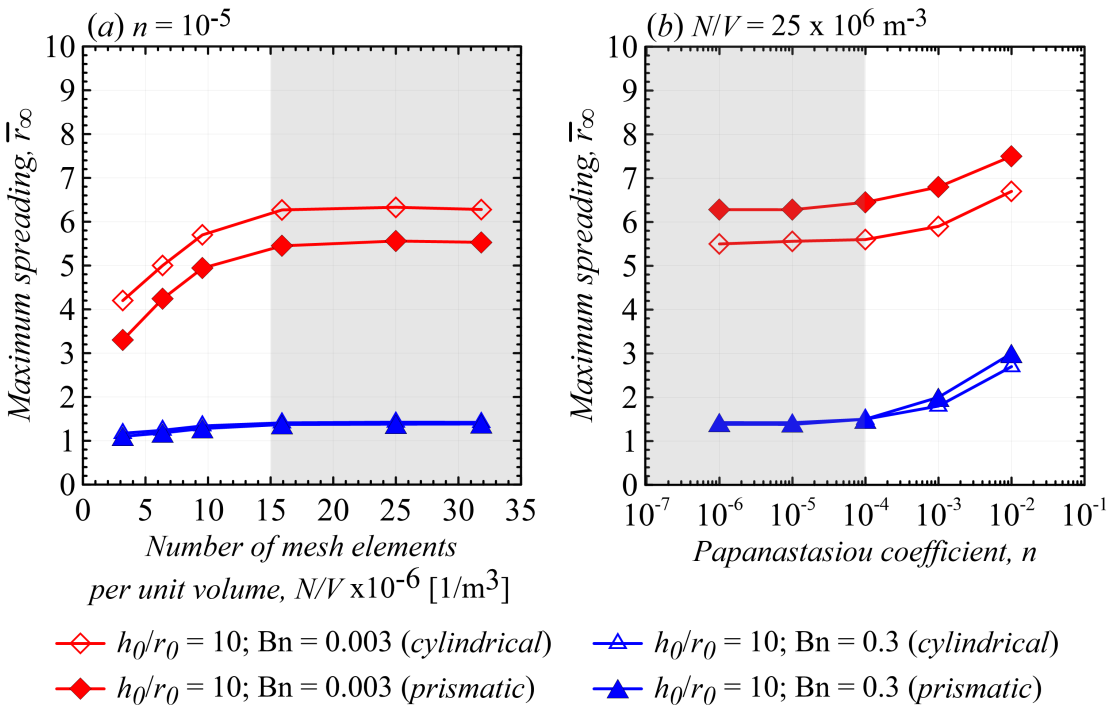

Fig. 19. A sensitivity study for the 3D Bingham dam-breaks considered in both Figs. 12 and 13: cylindrical column with $h_0/r_0 = 10$, Bn $= 0.003$ (opened red diamonds); prismatic column with $h_0/r_0 = 10$, Bn $= 0.003$ (solid red diamonds); cylindrical column with $h_0/r_0 = 10$, Bn $= 0.3$ (opened blue triangles); prismatic column with $h_0/r_0 = 10$, Bn $= 0.3$ (solid blue triangles). (a) Computations linking the maximum column spreading r_∞/r_0 with the number of mesh elements N per column unit volume V (N/V). (b) Impact of the Papanastasiou coefficient n on r_∞/r_0. Variations of r_∞/r_0 vanish within the gray regions.